

Simulating fully 3D non-planar evolution of hydraulic fractures

Sergey Cherny · Vasiliy Lapin · Denis Esipov ·
Dmitriy Kuranakov · Alexander Avdyushenko ·
Alexey Lyutov · Petr Karnakov

Received: 20 April 2015 / Accepted: 26 May 2016 / Published online: 4 July 2016
© Springer Science+Business Media Dordrecht 2016

Abstract Three-dimensional model of fracture propagation is proposed. The model simultaneously accounts rock deformation in the vicinity of a fracture and a cavity, fluid flow inside the fracture and its propagation in the direction that is selected by a growth criterion. The results of the sensitivity analysis of model solution to the variation of model parameters are presented.

Keywords 3D boundary element method · Fracture initiation · 2D fluid flow · Hydraulic fracture propagation · Numerical simulation · Fully coupled

1 Introduction

There are a lot of papers that concern modeling of hydraulic fracturing process, which started at 1950s. Review of the most widely-used one-, two-, and three-dimensional models is given in [Esipov et al. \(2014\)](#). Fully 3D models are distinguished among other because of their important distinctive feature which is the ability to describe out-of-plane propagation or in other words dimensional reorientation of a fracture. They describe not only opening mode, but also the relative shear displacement of crack edge, and are able to simulate fracture sliding and tearing. The typical case,

where such models are needed is when the initial fracture is not oriented in the preferred fracture plane and the final crack may result tortuous. Then, the restriction of the crack width near a wellbore may cause its further plugging by a proppant.

Before the simulation of fracture propagation itself, one needs to solve the problem of fracture initiation to obtain the initiation pressure, fracture position and orientation, which are the necessary initial data for the simulation of fracture propagation. The solution of 3D fracture initiation for the different cases is presented in [Esipov et al. \(2011a\)](#), [Alekseenko et al. \(2013\)](#), [Aidagulov et al. \(2015\)](#). It is shown that the fracture can initiate from a wellbore, an intersection between the wellbore and a perforation, and from the perforation itself. The conditions of each case execution are determined. In [Esipov et al. \(2011a\)](#) the influence of casing, which is the integral part of technological process, is also determined. It is shown that the presence of this column sufficiently changes both the initiation pressure and the initial fracture position.

The local condition when a critical tensile stress on a cavity surface exceeds the rock tensile strength is considered as the criterion of fracture initiation in above mentioned papers ([Esipov et al. 2011a](#); [Alekseenko et al. 2013](#)). Here, the cavity size is not directly taken into account.

However, the initiation pressure actually depends on the cavity geometry and in particular on its typical size ([Neuber 1937](#); [Novozhilov 1969](#)). The authors

S. Cherny (✉) · V. Lapin · D. Esipov · D. Kuranakov ·
A. Avdyushenko · A. Lyutov · P. Karnakov
Novosibirsk, Russia
e-mail: cher@ict.nsc.ru

of mentioned articles have introduced a linear size of the object problem. They have suggested comparing the segment-averaged mean tension stress σ with the critical stress σ_c . The segment-averaging procedure is performed over the interval of length d , which connects a point on the cavity and an adjacent point in an elastic media. In the paper (Novozhilov 1969), d is interpreted as an interatomic distance. It can also be interpreted as a typical size of a grain. The influence of a loaded specimen size has also been studied at experimentally-theoretical work (Carter 1992). In papers (Neuber 1937; Novozhilov 1969; Carter 1992) the size effect of a specimen has been considered in a two-dimensional initiation problem. Paper (Cherny et al. 2015) generalizes it to sufficiently three-dimensional fracturing problems. In that case, the value d is calibrated using an experimental data.

In the present paper, we focus on the simulation of the exclusively fully 3D (non-planar) evolution of hydraulic fractures. The suggested models and methods are the natural generalization of the approaches that have been developed by the authors in Cherny et al. (2009), Alekseenko et al. (2011).

2 The concept of mathematical model

In all of articles reviewed in the present paper, a fracture is considered without a cavity. Fluid injection is simulated as a point source at its surface. In the model which is described here we use the geometrical concept presented in Fig. 1, that connects the cavity and the frac-

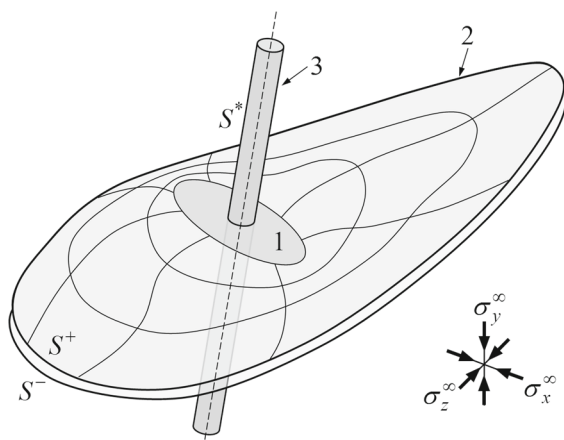


Fig. 1 Geometrical concept of 3D models: 1 initial fracture; 2 crack front; 3 cavity with border S^* ; S^\pm upper and bottom crack sides

ture. The fracture is considered as a curvilinear surface in three-dimensional infinite media that consists of the upper S^+ and the lower S^- sides. The surfaces S^+ and S^- are geometrically equal and the outer unit normal at coinciding points satisfies the expression $\mathbf{n}^+ = -\mathbf{n}^-$. It is observed that in the case of high stress in deep reservoirs and in case of low fluid viscosity the fluid pressure along the fracture faces is almost constant. Therefore, we will consider two models of fracture loading here.

In the first one we assume that the fluid pressure is constant along the fracture faces, although it can be time-dependent. Under this condition, it is also assumed that the fluid and the fracture fronts coincide, i.e. the size of so-called fluid lag is negligible. We will say that such hydraulic fracture propagation regime is described by a quasi-static crack growth model.

In the other model the viscous fluid flow inside the fracture is simulated. The flow of Newtonian fluid along the surface of fracture is described by 2D equations: the unsteady continuity equation and two simplified (lubrication theory) momentum equations.

The fracture grows in an isotropic homogeneous elastic material, compressed at the infinity by a stress tensor σ^∞ with principal components σ_x^∞ , σ_y^∞ , and σ_z^∞ . It is assumed that the fracture grows with a sufficiently low velocity, and the propagation can be described in the scope of linear elasticity fracture theory (Cherepanov 1979).

The present paper examines two hydraulic fracture propagation regimes which are the quasi-static fracture growth and the viscous fluid fracture growth. In the latter case, the propagation model is unsteady. The process unsteadiness is taken into account in the flow continuity equation. Meanwhile, all other equations describing the momentum balance, the elastic equilibrium, and the material breakage are stationary. The dynamics of propagation process is represented by the static conditions of flow momentum, stress field, and elastic media displacements in different moments of time.

3 Stress-displacement analysis of an elastic media near the cavity and the fracture

3.1 Governing equations

The stress-strain state of an isotropic homogeneous media is described by the elastic equilibrium equations

$$\frac{\partial \sigma_{ij}}{\partial x_j} = 0, \tag{1}$$

in which the components of stress tensor σ_{ij} satisfy the linear Hookes law in the case of small strains ε_{ij}

$$\sigma_{ij} = \lambda \delta_{ij} \varepsilon_{kk} + 2\mu \varepsilon_{ij}, \quad \varepsilon_{ij} = \frac{1}{2} \left(\frac{\partial u_i}{\partial x_j} + \frac{\partial u_j}{\partial x_i} \right). \tag{2}$$

In (2) u_i are the displacemnts, λ and μ are the Lamé parameters expressed via Young modulus E and Poisson’s ratio ν as

$$\lambda = \frac{E\nu}{(1+\nu)(1-2\nu)}, \quad \mu = \frac{E}{2(1+\nu)}. \tag{3}$$

Out of the equations (1) and (2) the Lamé’s equations of elastic equilibrium in terms of the displacements are derived (Sedov 1997)

$$(\lambda + \mu) \text{grad div} \mathbf{u} + \mu \Delta \mathbf{u} = 0, \tag{4}$$

where $\mathbf{u} = (u_1, u_2, u_3)$.

3.2 Boundary conditions

The inner boundary S problem (Fig. 1) consists of the cavity border S^* , upper S^+ and lower S^- fracture borders: $S = S^* + S^+ + S^-$.

On the cavity S^* the boundary condition

$$t_i \equiv \sigma_{ij} n_j = -p_{well} n_i - \sigma_{ij}^\infty n_j, \tag{5}$$

is set up, where n_i are the components of the surface outer unit normal; p_{well} is the pressure in the cavity; σ_{ij}^∞ are the components of tensor σ^∞ . The principal components σ_x^∞ , σ_y^∞ , and σ_z^∞ of tensor σ^∞ are applied in the directions of axis x , y and z respectively and are revealed as an in situ stress.

On the fracture surface S^\pm in the fracture propagation problem the following boundary condition is set

$$t_i = -p_{crack} n_i - \sigma_{ij}^\infty n_j. \tag{6}$$

There is also the condition at the infinite distance that should be satisfied

$$u_i(\infty) = 0. \tag{7}$$

The in situ stress is accounted by the terms σ_{ij}^∞ in the boundary conditions (5) and (6). The solution of the elasticity problem provides the stress-strain state of rock that is already strained with the stress σ_{ij}^∞ . Therefore, the actual stress that appear in the rock equals to the $\sigma_{ij} + \sigma_{ij}^\infty$.

3.3 Solution method

Essentially, two main methods for the solution of elasticity sub-problem are used in the papers that concern 3D initiation and evolution of hydraulic fractures: the finite element method (FEM) (Gupta and Duarte 2014) and the boundary element method (BEM). The prototype of the latter is the so-called “direct method” of linear elasticity based on Somigliana’s solution (Rizzo 1967). The FEM is employed to discretize the 3D partial differential equations. Then, the large volume of reservoir in the vicinity of the wellbore and the hydraulic fracture needs to be discretized. This is a very computationally expensive procedure. Therefore, in the problems of elasticity the BEM has gained popularity because of its boundary-only discretization that reduces the dimensionality of the problem (Rizzo 1967). The Conventional BEM (Rizzo 1967) can be implemented for the problems of fracture initiation from the cavity, which is confined by some surface S^* without any fractures (Aleksenko et al. 2013; Aidagulov et al. 2015; Briner et al. 2015a, b). However, using the conventional BEM to collocate the coincident points on the opposite crack surfaces produces a singular system of algebraic equations. The equations for a point, which is located at one of the surfaces of the crack, are identical to those equations for the point with the same coordinates, but at the opposite surface (Cruse 1972, 1973).

Many methods have been devised to overcome this difficulty. The crack Green’s function method (Snyder and Cruse 1975) is applied to the problems with a dominant crack of so regular a shape that free-space Green’s functions, which satisfies the traction-free boundary condition on the crack surface, is obtainable.

The multiple-zone method (Blandford et al. 1981) introduces artificial boundaries in the intact area to connect cracks and the boundary and thus divides the domain into zones so that no cracks appear in the interior of each zone. The drawback of the multiple-zone method is that the introduction of artificial boundaries is not unique, and thus cannot be easily implemented into an automatic procedure. In the problems of fracture propagation the remeshing of artificial boundary is required at every step of fracture growth. In addition, the method generates a larger system of algebraic equations than the required. Despite these drawbacks, the multiple-zone method has been the most widely used technique for elastostatics. In Esipov et al. (2011a, b) we used the multiple-zone BEM for the solution of

three-dimensional fracture initiation problem from the cased wellbore.

The displacement discontinuity method (DDM) was proposed by [Crouch \(1976\)](#). In this method, the unknown functions are the displacement discontinuities between the crack surfaces and can be used directly. In the original DDM for 2D elasticity problems, the displacement discontinuity across the two surfaces of a crack are assumed to be constant on line segments representing the crack. Stresses in the cracked domain are related to the displacement discontinuities on the line segments using the Papkovitch functions and superposition. In [Liu and Li \(2014\)](#) it is shown explicitly that the DDM is equivalent to the BEM, in which the traction (hypersingular) boundary integral equation (TBIE) is discretized with constant line elements instead of displacement (singular) boundary integral equation (DBIE). In the one of the first papers on the simulation of fully three-dimensional fracture propagation ([Vandamme and Curran 1989](#)) the DDM was used for solving the hydraulic fracturing problem. The borehole, through which the fluid is injected into the fracture is not simulated in the stress analysis: its size is assumed to be negligible, compared to the size of the fracture.

In [Napier and Detournay \(2013\)](#) the initial propagation of fractures from a pressurized borehole in three-dimensional case is simulated. In the present paper in order to apply the DDM to a borehole-fracture problem the borehole is represented as a cylindrical crack and it comprises displacement discontinuity elements. I.e. a fictive body that has the same properties as an external elastic media is placed into a borehole. The solutions of the external and the fictive internal problems are simultaneously found. The displacements of some points of the fictive body should be fixed to avoid its shift and rotation as a rigid body even if only the external problem is of interest. The displacements in the fictive body are defined using these fixed points and in the external domain they are defined using fixed zero displacements at the infinity. If the problem under consideration has two planes of symmetry as in [Napier and Detournay \(2013\)](#) then the internal domain is automatically fixed with regard to these two planes. If the problem under consideration is not symmetrical, then additional elements should be added in to the crack and zero displacements should be set at their inner sides to prevent the motion of the internal domain as a rigid body. These elements can produce additional stresses that can affect

the solution of the external problem. The resulting solution of external problem will not be equal to the correct solution of the original problem obtained for example by the dual boundary element method (DBEM).

The most suitable method for the solution of the elasticity problem in 3D model of fracture propagation from the arbitrary cavity is the DBEM ([Hong and Chen 1988](#); [Chen and Hong 1999](#)). The first use of dual integral equations in crack problems has been reported by [Bueckner \(1973\)](#). [Watson \(1982, 1986\)](#) has presented the normal derivative of the displacement boundary integral equation for the development of Hermite cubic element where the number of unknowns is larger than the number of equations. For the case of a degenerate boundary, the dual integral representation has been proposed for crack problems in elasticity by [Hong and Chen \(1988\)](#), [Chen and Hong \(1999\)](#). They have introduced the idea of dual boundary integral equation, in which a combination of the standard boundary integral equation and its derivative can be used to provide independent equations in order to overcome the problem of degeneracy. Hong and Chen have presented the theoretical basis of dual integral equations having shown how the DBIE can be differentiated and Hooke's law can be applied to derive the TBIE. [Portela et al. \(1991\)](#) have implemented the combined use of the DBIE and the TBIE in single system to solve two-dimensional linear elastic crack problems. Both of the crack surfaces are discretized with discontinuous quadratic boundary elements, in which nodes are located within the body of element. The collocation at these nodes satisfies the Holder continuity requirements of the hypersingular integral equation since the shape functions are continuously differentiable at these points. [Mi and Aliabadi \(1992, 1994\)](#) has extended two-dimensional cases to the three-dimensional crack problems.

The difficulties in using DBEM in comparison with the conventional BEM are the high degree of the singularity of TBIE and the increase of computational costs because of the necessity to use discontinuous boundary elements, which leads to the increase of the degrees of freedom, and as result to the enlargement of matrix in SLAE.

In our work, we develop another approach that still allows to use the conventional BEM by the means of a slight modification of the computational domain. In this approach the real fracture is replaced by a fictitious notch with an artificial finite width d_{art} (Fig. 2). The artificial width parameter should be chosen to min-

imize the error caused by domain modification. The collocation nodes at the opposite sides of the notch are positioned far enough to make the algebraic equations well-conditioned and close enough to keep the errors of the calculation of crack width and stress intensity factors minimal. The appropriate value of the parameter and the estimation of the computational error caused by the BEM with domain modification (BEM/DM) are presented further. The artificial notch approach based on the conventional BEM has computational advantages comparing to both DDM and DBEM. Indeed, let the cavity surface be presented by N_c elements and the fracture be presented by N_f elements. As it has been mentioned, the discontinuous boundary elements should be used for the hypersingular TBIE discretization and the continuous elements can be used for the DBIE discretization. In the case of the simplest linear elements the following degrees of freedom can be estimated for the given methods. The DDM produces a system of linear equations with $3(4N_f + 4N_c)$ degrees of freedom, the DBEM gives $3(4N_f + N_c)$ degrees of freedom and BEM/DM gives $3(2N_f + N_c)$ degrees of freedom. From the given estimations, it is clear that the suggested BEM/DM is the most suitable method for a 3D elasticity problem from the computational point of view. Especially, if the crack sizes are significant and N_f values are correspondingly significant too.

4 Crack growth model

4.1 Stress intensity factors and the specific features of their calculations

The fundamental postulate of Linear Elastic Fracture Mechanics (LEFM) is that the behaviour of cracks is determined solely by the value of Stress Intensity Factors (SIFs). The stress field in the vicinity of the crack front is characterized by the SIFs K_I , K_{II} and K_{III} . In the present paper, the displacement extrapolation method for evaluating SIFs is employed (Aliabadi 2002)

$$\begin{aligned}
 K_I^O &= \frac{E}{4(1-\nu^2)} \sqrt{\frac{\pi}{2l}} \left(u_b^{P^+} - u_b^{P^-} \right), \\
 K_{II}^O &= \frac{E}{4(1-\nu^2)} \sqrt{\frac{\pi}{2l}} \left(u_n^{P^+} - u_n^{P^-} \right), \\
 K_{III}^O &= \frac{E}{4(1+\nu)} \sqrt{\frac{\pi}{2l}} \left(u_t^{P^+} - u_t^{P^-} \right),
 \end{aligned}
 \tag{8}$$

where point O is at the crack front; the displacements \mathbf{u}^{P^+} and \mathbf{u}^{P^-} are evaluated at the points P^+ and P^- , which are the nodes in the neighbourhood of the crack front for the upper and lower crack surfaces, respectively; u_b, u_n and u_t are the projections of \mathbf{u} on the coordinate directions of the local crack coordinate system presented in Fig. 3, and l is the distance to the crack front.

Let us evaluate the accuracy of SIFs calculations using the formula (8) on an inclined penny-shaped crack problem. There is a penny-shaped fracture of radius R , upper S^+ side, lower side S^- , and a center in the origin of coordinates. This crack is placed on a plane which is inclined at an angle α to the axis Oz (Fig. 4a). The surrounding media is loaded at the infinity by uniaxial tensile stress σ^∞ with principal components $\sigma_x^\infty = \sigma_z^\infty = 0, \sigma_y^\infty > 0$. Stresses on the fracture sides are equal to zero $\sigma \cdot \mathbf{n} \Big|_{S^\pm} = 0$.

The exact solution for the SIFs is (Murakami 1987; Tada et al. 2000)

$$K_I = 2\sigma_y^\infty \cos^2 \alpha \sqrt{\frac{R}{\pi}}, \tag{9}$$

$$K_{II} = \frac{4}{2-\nu} \sigma_y^\infty \sin \alpha \cos \alpha \cos \omega \sqrt{\frac{R}{\pi}}, \tag{10}$$

$$K_{III} = \frac{4(1-\nu)}{2-\nu} \sigma_y^\infty \sin \alpha \cos \alpha \sin \omega \sqrt{\frac{R}{\pi}}, \tag{11}$$

where ω is an angular coordinate on the crack plane that represents a position of the crack front.

For a particular case when $\alpha = 0$, the fracture propagation problem has an exact solution (Sneddon and Elliott (1946); Abe et al. (1976))

$$W(\sigma_y^\infty, r) = \frac{8\sigma_y^\infty}{\pi E'} \sqrt{R^2 - r^2}, \tag{12}$$

where W is the fracture width, calculated using the formula $W(\mathbf{x}) = \mathbf{u}^+(\mathbf{x}^+) \mathbf{n}^+(\mathbf{x}^+) + \mathbf{u}^-(\mathbf{x}^-) \mathbf{n}^-(\mathbf{x}^-)$, $\mathbf{x} = \mathbf{x}^\pm \in S^\pm$ (Fig. 2), E' is the plane strain modulus, associated with the Young modulus E and the Poisson's ratio ν

$$E' = \frac{E}{1-\nu^2}. \tag{13}$$

Figure 5 shows the numerical fracture width calculated with the BEM/DM (Fig. 4b) under parameters $\alpha = 0, R = 1$ m, $\sigma_y^\infty = 1$ MPa, $E = 20$ GPa, $\nu = 0.2$, and the exact (12). The computational mesh contains 16 elements in radial direction r and 64 elements in circumferential direction ω . The artificial notch width equals $d_{art} = 0.12$ m.

Fig. 2 Artificial notch concept: real fracture (left) is replaced with artificial notch (right)

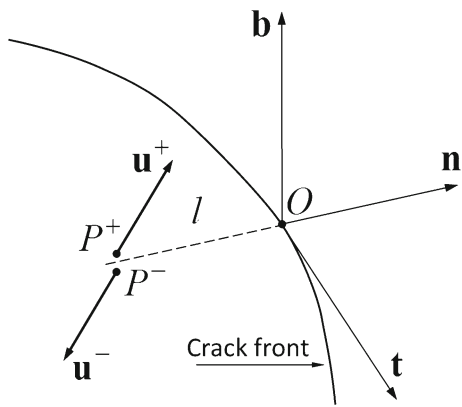
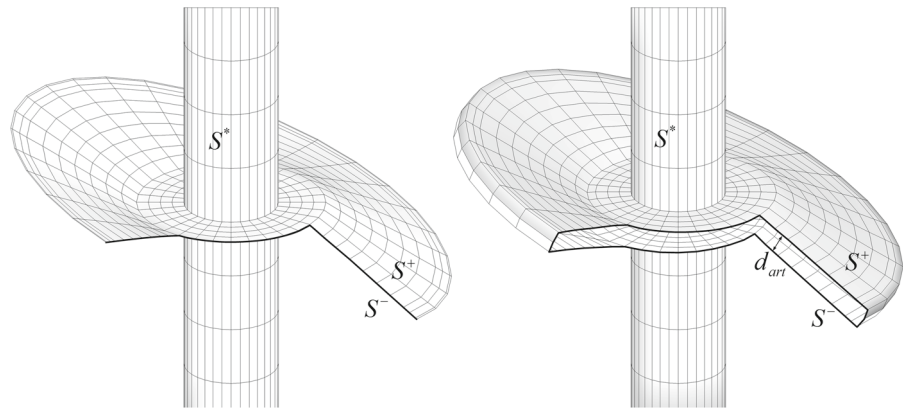


Fig. 3 Evaluation of stress intensity factors from nodal displacements

Let us consider now the influence of displacements calculation on K_I value. In Fig. 6 the values of K_I for the problem with the parameters mentioned above,

calculated at each mesh node along the radius, using the first formula (8) are shown. The displacements are taken from the exact and the numerical solutions using the BEM/DM method with $d_{art} = 0.12$ m. It can be seen that the accuracy of K_I calculations the by single-point formulae (8) reduces at the three nodes nearest to the crack front. The following approach for the calculation of all SIFs at the crack front K^0 is proposed here.

Let us assume that on the propagation step n the front has an increment in a form of a ruled surface Z and the fracture propagates to the step $n + 1$ as it is shown in Fig. 7. The lengths of the ruled surface L are the fracture increment magnitudes. In the suggested approach, SIFs at \mathbf{x}^{n+1} are calculated using only the displacements from the fracture increment Z . The surface Z is divided into $N_f + 1$ auxiliary circular layers

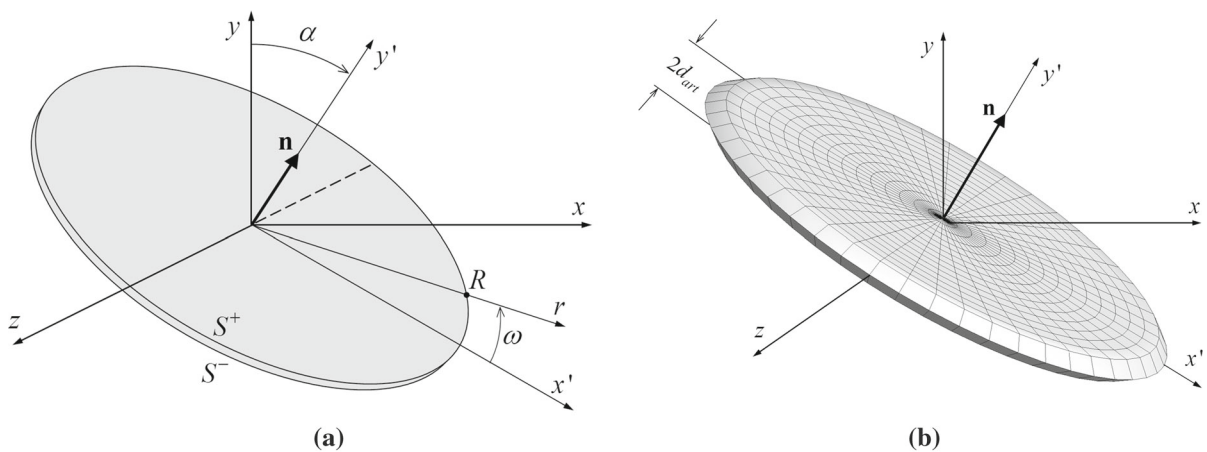


Fig. 4 The problem of penny-shaped crack in a media stretched in the direction of coordinate y : **a** infinitely thin fracture in a plane rotated around axis Oz by an angle of α ; **b** penny-shaped notch of width $2d_{art}$ with sharp tip in the same plane

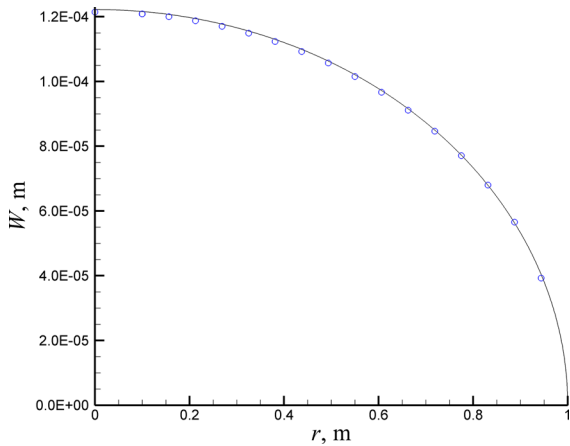


Fig. 5 Fracture width profiles: exact solution (12) (solid line); BEM/DM with $d_{art} = 0.12$ m (circle)

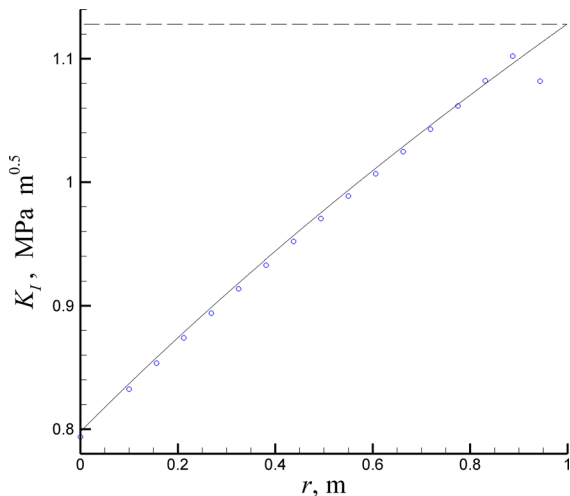


Fig. 6 SIF K_I : formula (9) with $\alpha = 0$ (dashed); first formula (8) in mesh nodes with displacements taken from (12) (solid line) and numerical solution BEM/DM with $d_{art} = 0.12$ m (circle)

of elements. The width of front-line element is L_f , the width of all other elements is $(L - L_f)/N_f$. After the calculation of fracture’s nodes \mathbf{x}^{n+1} on step $n + 1$, and after the transition to the step $n + 2$ of propagation, auxiliary layers are erased from the memory.

For the SIFs calculations at the point O of the crack front the two-point formula is used

$$K^O = K^2 + \frac{l_2(K^1 - K^2)}{l_2 - l_1}, \tag{14}$$

where K^1 and K^2 are the each of three SIFs, calculated using the formulae (8) at the nodes 1 and 2 of the auxiliary layer of elements, which is the most distant from

crack front $N_f + 1$ (see Fig. 7); l_1 and l_2 are the distances between the front and the nodes 1 and 2 respectively. In all the further calculations the following values were considered $N_f = 3$, $L_f = 0.2L$.

Figure 8 shows the dependencies of the SIFs along the crack front for a penny-shaped crack inclined at $\alpha = 45^\circ$, obtained from the exact solution (9)–(11) and another obtained using the suggested numerical approach.

4.2 Crack growth criteria

Several criteria have been proposed to describe the magnitude of the crack front advance at each crack front vertex. Among them, the most popular are the maximum energy release rate criterion and the modified fatigue criterion based on the Paris-Erdogan formula. The suggested model includes both of these criteria and it might be used for simulation either brittle or fatigue fracturing.

4.2.1 The strain energy release rate criterion

The classical formulation of the strain energy release rate criterion for the spatial mixed mode loading fractures (Nuismer 1975; Germanovich and Cherepanov 1995; Weber and Kuhn 2008; Gupta and Duarte 2014) consists in the following. The fracture propagates when the energy release rate in the direction of crack propagation θ^* reaches the critical energy release rate of the material (G -criterion)

$$G(\theta^*, t + \Delta t) = G_c, \tag{15}$$

where

$$G(\theta^*, t + \Delta t) = \frac{1 - \nu^2}{E} \left(K_I^2(\theta^*, t + \Delta t) + K_{II}^2(\theta^*, t + \Delta t) \right) + \frac{1 + \nu}{E} K_{III}^2(\theta^*, t + \Delta t),$$

$$G_c = \frac{1 - \nu^2}{E} K_{Ic}^2,$$

t is the time before kinking, Δt is time increment for the transition to the next crack front position, θ^* is the kinking angle.

In the present manuscript the Maximum Tangential Stress (MTS) criterion (Erdogan and Sih 1963) is used to define the fracture propagation direction θ^* . For the

Fig. 7 Ruled surface of fracture increment Z between propagation steps n and $n + 1$

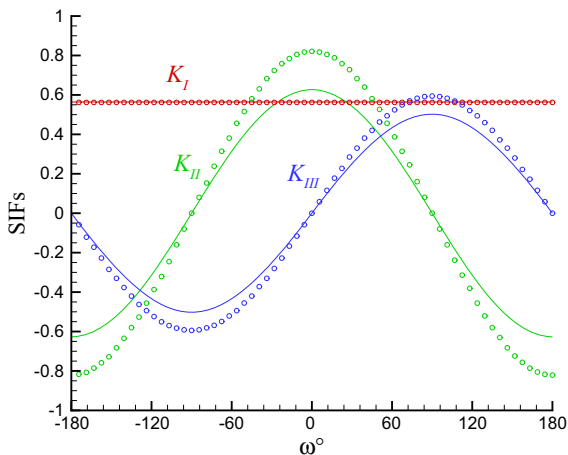
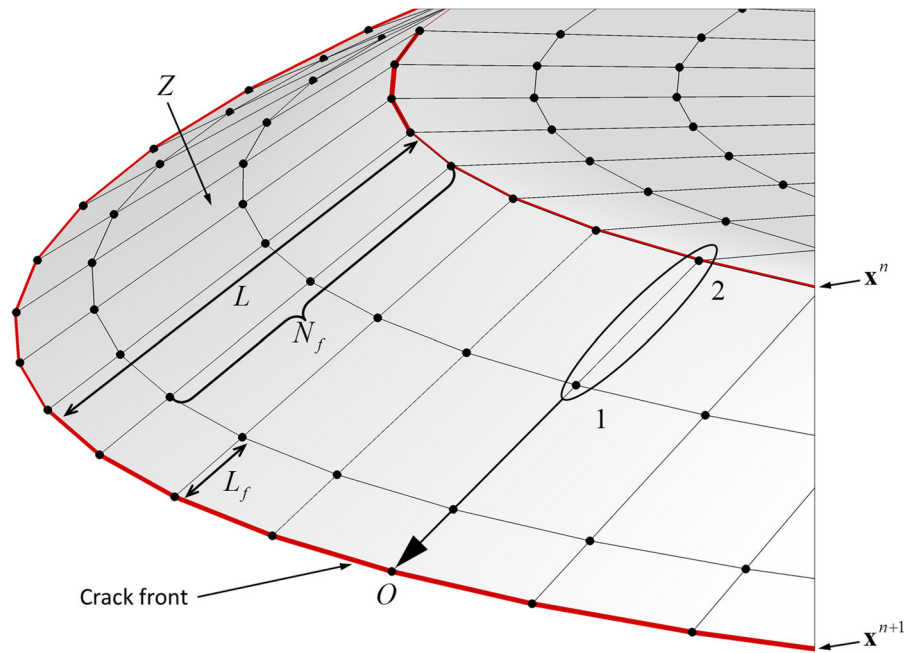


Fig. 8 SIFs variation along the penny-shaped crack inclined at 45° : exact solution (solid line); BEM/DM with $d_{art} = 0.12$ m (circle)

explicit calculation of θ^* in plane mixed-mode crack problem MTS gives

$$\theta^* = 2 \arctan \left(\frac{K_I(t) - \sqrt{K_I^2(t) + 8K_{II}^2(t)}}{4K_{II}(t)} \right). \quad (16)$$

The implicit condition for the calculation of θ^* is used, which is equivalent to the MTS criterion

$$K_{II}(\theta^*, t + \Delta t) = 0. \quad (17)$$

By taking into account the formula (17) in the equation (15) the strain energy release rate criterion (15) is transformed into the condition

$$K_I^2(\theta^*, t + \Delta t) + \frac{1}{1 - \nu} K_{III}^2(\theta^*, t + \Delta t) = K_{Ic}^2. \quad (18)$$

The influence of mode III in (18) on a fracture path diminishes with every new fracture propagation step because the fracture reorients to the Preferred Fracture Plane (PFP). Figure 9 shows the fracture paths, Fig. 10 shows the pressure distribution on propagation steps, Figs. 11 and 12 show the SIFs along the crack front, calculated using the G -criterion (15) and K_I -criterion

$$K_I(\theta^*, t + \Delta t) = K_{Ic}. \quad (19)$$

Thus, if the condition (17) is used to define crack front deflection then the implicit criteria (15) and (19) give similar results. If these criteria (15) and (19) were treated as explicit ones by using the explicit terms $K_{I,II,III}(t)$ instead of the implicit ones $K_{I,II,III}(\theta^*, t + \Delta t)$ then the results would be different. The problems described by by Leblond and Frelat (2000, 2001, 2004) and Dobroskok et al. (2005) can be used to demonstrate this difference.

In these articles the problems of sliding fractures under compressive loads are considered. In these problems the stress-strain state near the fracture tip at the

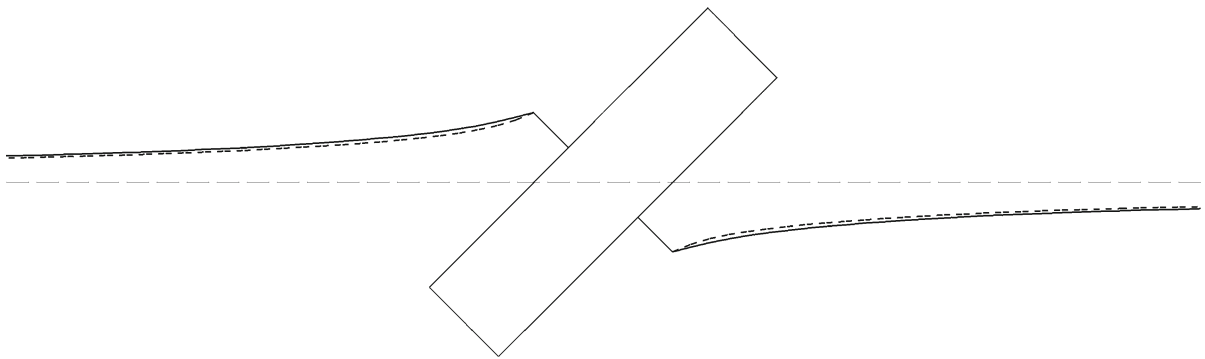
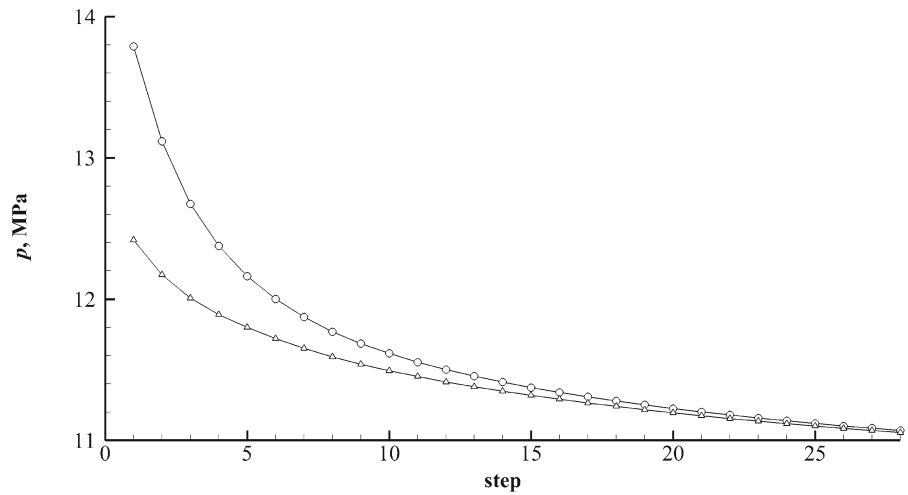


Fig. 9 Inclined at $\alpha = 45^\circ$ penny-shaped crack and cylindrical wellbore (cut through at the center of the domain): *solid line* K_I -criterion; *dashed line* G -criterion

Fig. 10 Pressure versus step of propagation: *circle* K_I -criterion; *triangle* G -criterion



moment t before the fracture propagation is characterized by zero mode I and non-zero mode II

$$K_I(t) = 0, K_{II}(t) \neq 0. \tag{20}$$

Therefore, the explicit criterion (19) in contrast to (15) is not fulfilled. But if one considers both criteria at the moment $t + \Delta t$ after the fracture kinking then according to the principle of local symmetry (Goldstein and Salganik 1974) mentioned in Leblond and Frelat (2001) the following relationships will be valid

$$K_I(t + \Delta t) > 0, K_{II}(t + \Delta t) = 0. \tag{21}$$

In this case the implicit criteria (15) and (19) are equivalent. Besides that there is no mode III in the problems that are considered in Leblond and Frelat (2000, 2001, 2004), Dobroskok et al. (2005).

Note that according to Richard et al. (2005) the criteria of Erdogan and Sih (1963), Nuismer (1975), Richard et al. (2005) and Schollmann et al. (2002) should be

used very carefully while being applied to the cases like the sliding of cracks under pure mode II or III loading. This means that the criterion (19) may be non-applicable for the problems described by Leblond and Frelat (2000, 2001, 2004). However, in the problems of pressurized fracture (that are considered in the present paper) the fracture is always opened, therefore the SIF mode I is greater than zero and the mentioned criteria are applicable.

4.2.2 The modified fatigue criterion based on the Paris-Erdogan formula

The Paris-Erdogan fatigue law is discussed in the manuscript as an alternative to the iterative selection method of crack front increment calculation which satisfies K_I or G —criteria.

Fig. 11 SIFs along crack front at various steps of propagation with K_I -criterion: circle step 2, triangle step 10, square step 28

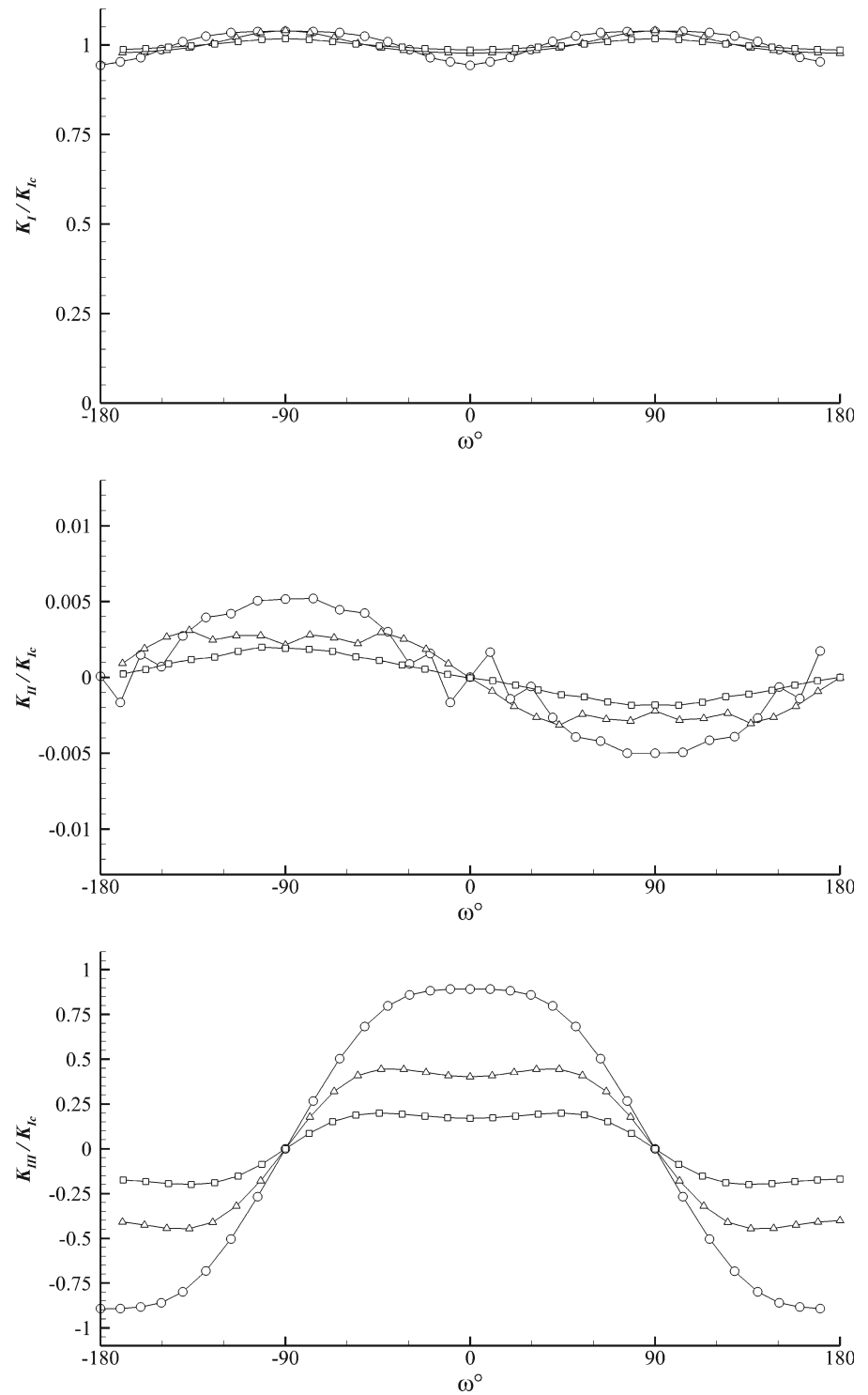
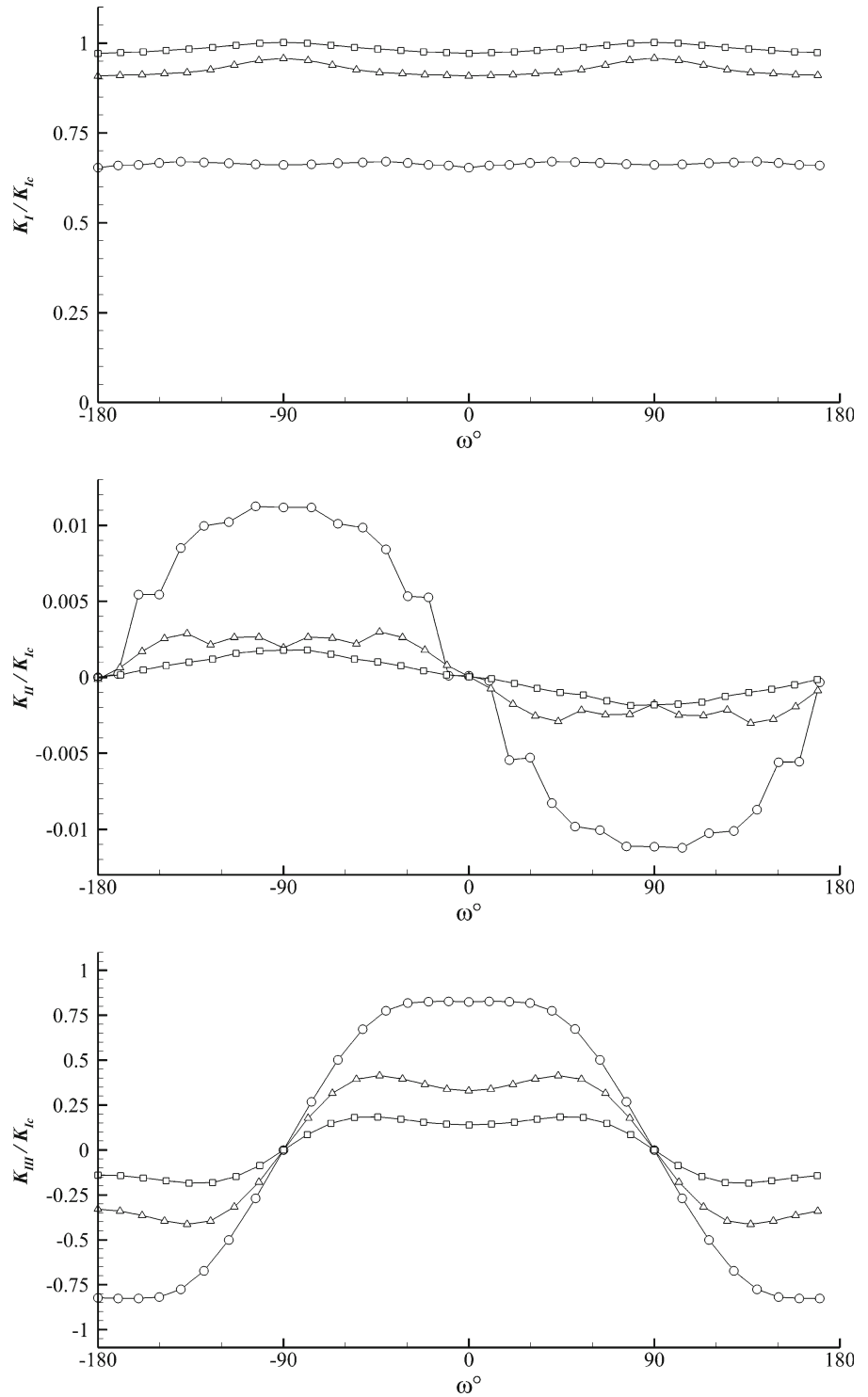


Fig. 12 SIFs along crack front at various steps of propagation with G -criterion: *circle* step 2, *triangle* step 10, *square* step 28



The Paris-Erdogan model is used to simulate the fatigue crack propagation, which states that

$$\frac{dL}{dN} = C(\Delta K_{eq})^m, \tag{22}$$

where dL/dN is the rate of crack propagation with respect to the number of loading cycles; C and m are the material constants;

$$\Delta K_{eq} = K_{eq}^{max} - K_{eq}^{min} = K_{eq}^{max}(1 - R) \tag{23}$$

in which K_{eq} is the effective stress intensity factor, adopted in Richard et al. (2005) as

$$K_{eq} = \frac{K_I}{2} + \frac{1}{2}\sqrt{K_I^2 + 4(\alpha_1 K_{II})^2 + 4(\alpha_2 K_{III})^2} \tag{24}$$

with $\alpha_1 = 1.155$ and $\alpha_2 = 1$. Since the linear elasticity is considered, R in (23) can be written as

$$R = \frac{K_{eq}^{min}}{K_{eq}^{max}} = \frac{\sigma_{min}}{\sigma_{max}}, \tag{25}$$

where σ_{min} is zero and σ_{max} is constant in Mi and Aliabadi (1994), Aliabadi (2002), Rungamornrat et al. (2005), Gupta and Duarte (2014). The formula for the crack front increment magnitude $L(l)$ from a time step t to $t + \Delta t$ at any point along the crack front l (Fig. 13) is derived from the law (22). The maximum value L^{max} of the next increment is the model parameter and it corresponds to the crack front point where the maximum ΔK_{eq}^{max} occurs. From (22) one can derive

$$L \approx C(\Delta K_{eq})^m N \tag{26}$$

and

$$L^{max} \approx C(\Delta K_{eq}^{max})^m N. \tag{27}$$

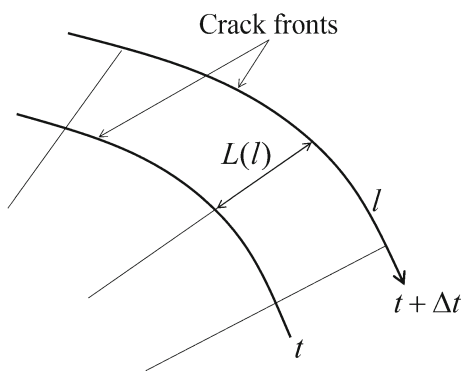


Fig. 13 Crack front increment $L(l)$ from a time step t to $t + \Delta t$

From (26) and (27) the following relationship is obtained

$$\frac{L}{L^{max}} = \left(\frac{\Delta K_{eq}}{\Delta K_{eq}^{max}} \right)^m. \tag{28}$$

Therefore, the incremental size at any front point l can be evaluated by

$$L(l) = L^{max} \left(\frac{\Delta K_{eq}}{\Delta K_{eq}^{max}} \right)^m \tag{29}$$

or with regard to the (23) and (25) it is approximately assumed that

$$L(l) = L^{max} \left(\frac{K_{eq}}{K_{eq}^{max}} \right)^m. \tag{30}$$

Formula (30) is called the scaling law for the crack front increment. In the present article one more assumption was made in (30) when replacing K_{eq} with K_I .

In Fig. 14 the comparison of the fracture trajectories of unloaded inclined penny-shaped fracture in a tensioned infinite media is presented. The results were obtained using the K_I criterion and the condition (17), as well as the scaling law (30) and the condition (16).

Also, the scaling law for the crack front increment value (30) was used to solve the problem of two parallel circle incipient fractures propagation (Fig. 15). The radii of the incipient fractures are 1 m, the distance between them is 0.4 m, constants are $m = 2.1$, $L^{max} = 0.1$ m. The problem is solved in the fatigue crack growth approximation in two statements: the non-loaded fractures ($p = 0$) are propagating in media under tensile stress $\sigma^\infty = 1$ MPa; the fractures loaded by pressure $p = 1$ MPa are put into the media with zero stress at infinity $\sigma^\infty = 0$. The criterion (17) is used to define the direction of crack front propagation. Increment value is calculated from (30).

4.2.3 Crack front deflection criterion

In many papers devoted to the prediction of three-dimensional crack growth (Vandamme and Curran 1989; Barr 1991; Sousa et al. 1993; Carter et al. 2010; Rungamornrat 2004; Rungamornrat et al. 2005) the crack front deflection is defined by only one kinking angle θ disregard the mode III (Fig. 16, a). They use the MTS criterion proposed by Erdogan and Sih (1963) for the calculation of kinking angle θ in plane mixed-mode problems. The kinking angle θ is calculated either using the formula (16) or implicitly from the condition (17).

Fig. 14 Inclined at $\alpha = 45^\circ$ penny-shaped crack (cut through at the center of the domain): $K_I = K_{Ic}$, $K_{II} = 0$ (dashed line) and (29), (16) (solid line) conditions

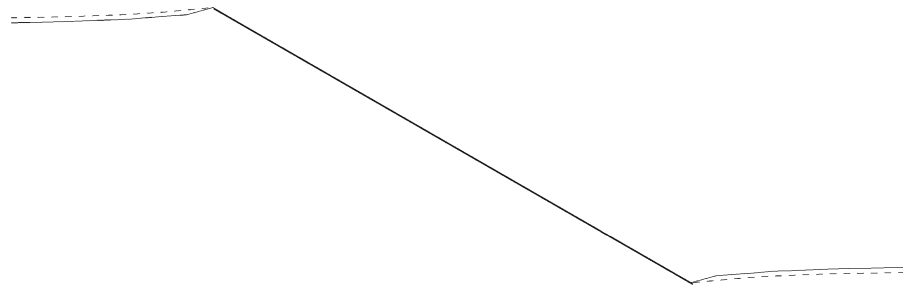
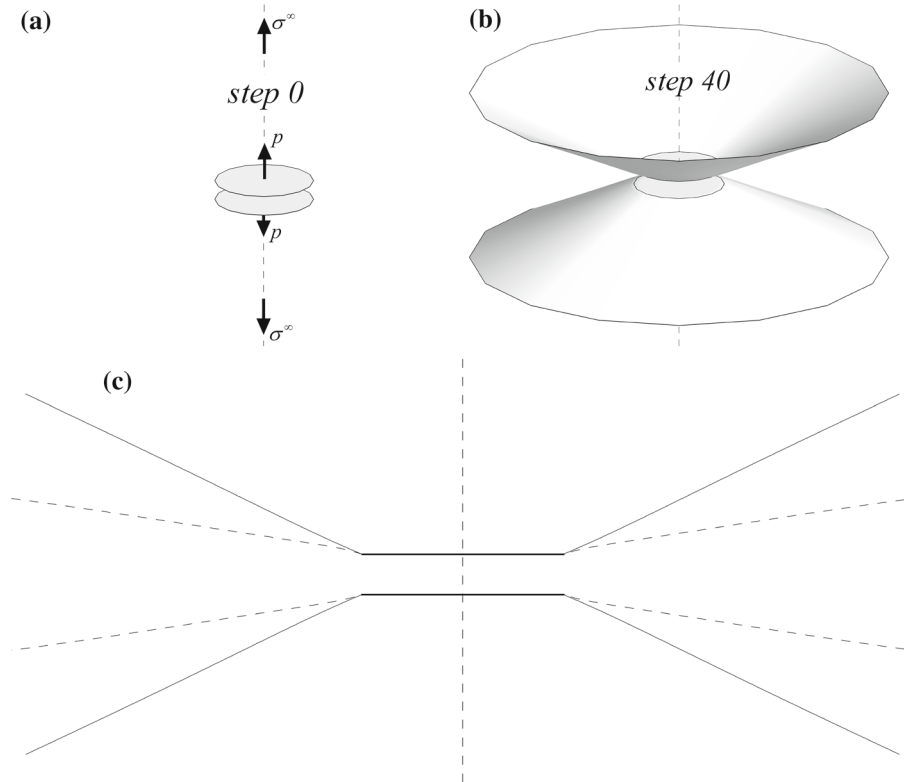


Fig. 15 Fracture propagation from the two parallel circle fractures: **a** initial fractures at step 0; **b** isometry of fractures loaded by $p = 1$ MPa in unloaded media $\sigma^\infty = 0$ at step 40; **c** paths of loaded by $p = 1$ MPa fractures in unloaded media $\sigma^\infty = 0$ (solid line) and unloaded ($p = 0$) fractures in tensile media $\sigma^\infty = 1$ MPa (dashed line)



The plane mixed mode criteria (15) (or (19)) and (16) (or (17)) has been used here as a very first approach of determining the crack front growth and deflection. However for realistic determination of crack paths in arbitrary 3D problems of real structures it is necessary to apply three-dimensional mixed-mode *I*, *II* and *III* criteria (Cooke and Pollard 1996; Richard et al. 2005) (Fig. 16, b). The kinking angle θ and the twisting angle ψ define the direction of crack front propagation at each front point l . We suggest the new crack front kinking and twisting model for three-dimensional mixed-mode case. To define the kinking and twisting angles it uses conditions

$$K_{II}(\theta(l)) = 0, \quad K_{III}(\psi(l)) = 0. \tag{31}$$

The angles θ and ψ are interconnected as it is shown in Fig. 17. It is possible to write down the formula which defines this connection

$$\tan \psi = \frac{L(\sin(\theta + \Delta\theta) - \sin \theta)}{\Delta l}. \tag{32}$$

By assuming the smallness of ψ , θ , $\Delta\theta$ and Δl values in (32), the dependence of the twisting angle from the derivative of kinking angle with respect to the coordinate l along the crack front can be obtained

$$\psi(l) = \frac{L(l)\Delta\theta}{\Delta l} = L(l)\frac{\partial\theta}{\partial l}(\theta(l)). \tag{33}$$

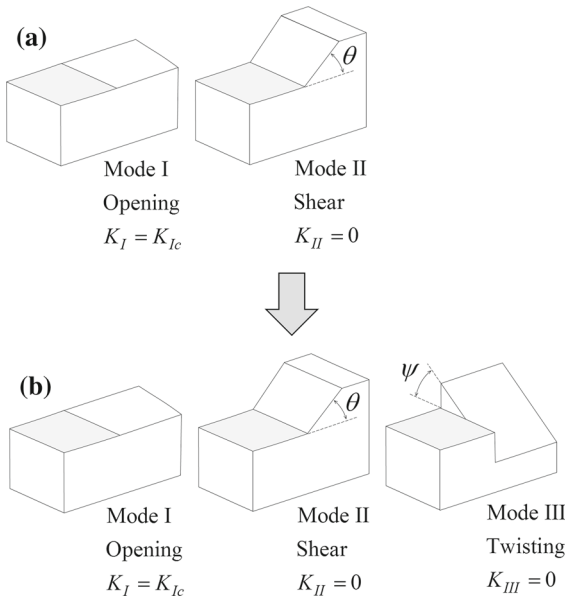


Fig. 16 Crack growth criterion and crack front deflection: **a** plane mixed mode; **b** spatial 3D mixed mode

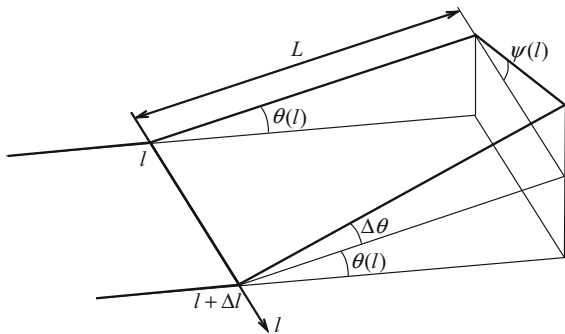


Fig. 17 The kinking angle θ and the twisting angle ψ define the direction of crack front propagation

Therefore, the third mode can be written as a function of the kinking angle

$$K_{III}(\psi(l)) = \bar{K}_{III}(\theta(l)). \tag{34}$$

It allows to rewrite the conditions (31) only for this angle θ

$$K_{II}(\theta(l)) = 0, \quad \bar{K}_{III}(\theta(l)) = 0. \tag{35}$$

It is impossible to fulfill the second condition in (35) at each point of the crack front separately from the adjacent points because the \bar{K}_{III} depends on the kinking angle θ derivative with respect to the l (33). Therefore, we have combined both modes K_{II} and K_{III} with weight β into a single function and have considered

this function as the integral along the whole crack front at new time step $t + \Delta t$

$$F(t + \Delta t, \theta(l)) = \int_{\text{Crack front}} (1 - \beta) K_{II}^2(t + \Delta t, \theta(l)) + \beta \bar{K}_{III}^2(t + \Delta t, \theta(l)) dl. \tag{36}$$

The crack front deflection in a 3D mixed mode criterion is determined by the distribution of $\theta^*(l)$ giving minimum F

$$F(t + \Delta t, \theta^*(l)) = \min_{\theta(l)} F(t + \Delta t, \theta(l)). \tag{37}$$

The optimization problem (37) is solved iteratively

$$F^{s+1} = \sum_{j \in \text{Crack front}} (1 - \beta) \left(K_{IIj}^s + \frac{1}{\alpha_{II}} \Delta^s \theta_j \right)^2 + \beta \left(\bar{K}_{IIIj}^s + \frac{L_j}{\alpha_{III}} \frac{\Delta^s \theta_{j+1} - \Delta^s \theta_j}{l_{j+1} - l_j} \right)^2, \tag{38}$$

where $\Delta^s \theta_j = \theta_j^{s+1} - \theta_j^s$ and s is the iteration index.

At each iteration $s + 1$ the angles θ_j^{s+1} are obtained as the points of the minimal value of functional (38) by solving the SLAE

$$\frac{\partial F^{s+1}}{\partial \theta_j^{s+1}} = 0, \quad j \in \text{Crack front}. \tag{39}$$

Parameter β allows to consider various propagation criteria. In case when $\beta = 0$ the maximal tangential stress (MTS) criterion is obtained. Nowadays, there is no agreement in choosing the most adequate three-dimensional propagation criteria (Richard et al. 2005), therefore the problem statement (36), (37) is used in a general form. Parameter β can be calibrated on different considered experimental problems.

To show the influence of K_{III} mode on the shape of crack front, an inclined penny-shaped crack propagation has been simulated. The initial crack inclination angle is $\alpha = 50^\circ$. The media is loaded by $\sigma_x^\infty = -16$ MPa, $\sigma_y^\infty = -10$ MPa, $\sigma_z^\infty = -16$ MPa. The fracture obtained using the described criterion for $\beta = 0.5$ is shown in Fig. 18. The fracture trajectories for the different weighting coefficient β in a plane cut through the center of the domain are shown in Fig. 19.

The distributions of three SIF modes along the crack front at various time steps for $\beta = 0.5$ are shown in Fig. 20. It is seen that the zero condition for the

Fig. 18 Fracture shape for the middle value of the weighting coefficient $\beta = 0.5$

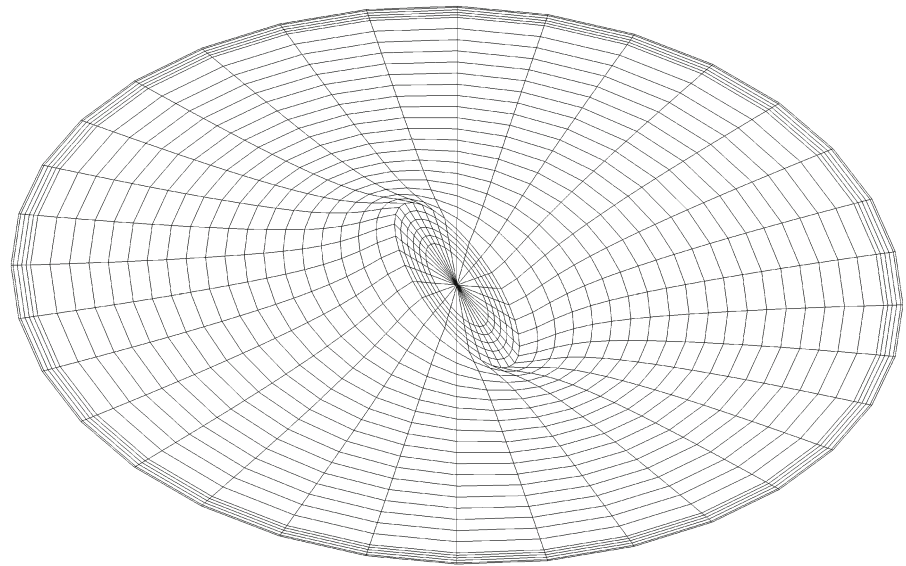
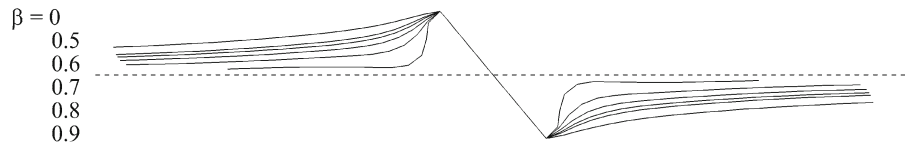


Fig. 19 Inclined at $\alpha = 50^\circ$ penny-shaped crack for different values of the weighting coefficient β



SIFs mode *II* and *III* is not fulfilled because the crack front can not twist enough to eliminate shearing stresses and displacements in its vicinity so fast. With the further fracture growth the front tends to a flat curve (Fig. 18) and the values of K_{II} , K_{III} are being reduced (Fig. 20).

At the present, there is no final formulation of the criterion that would allow to fix the adequate value of the weighting parameter β (Richard et al. 2005). Therefore various weighting parameters have been used. The SIFs distributions along the front at the 30th step of propagation are shown in Fig. 21 for the various values of weighting parameter β . It is seen that the plane mixed-mode model ($\beta = 0$) gives non-zero SIFs mode *III*. Although it should be zero at the plane crack front. If mode *III* is taken into account ($\beta \geq 0.5$) the values of the SIFs mode *III* become lower because of the smaller deflection of the fracture from the plane.

In this problem one cannot obtain the feather crack and the zigzag-shaped distribution of K_{III} along the crack front. The obtained K_{III} distribution is smooth which is also mentioned in Cooke and Pollard (1996); Pereira (2010). Nevertheless, the 3D mixed-mode *I*, *II* and *III* criteria mechanism is included in our model.

5 Fracture load

The two types of fracture load, and therefore – two hydraulic fracture propagation regimes are considered. They are the quasi-static crack growth and the viscous fluid crack growth.

5.1 Quasi-static crack growth

5.1.1 Unloaded fracture in an elastic media under tensile stress

The problem statement for the inclined penny-shaped crack was introduced in section 4.1. For the case of $\alpha = 0$ it is easy to obtain the analytic law of brittle quasi-static plane-radial fracture propagation. Let the initially set value of tension pull σ_y^∞ fulfill the condition

$$K_I < K_{Ic}, \tag{40}$$

and it is not propagating. At the same time, the fracture's width $W(\sigma_y^\infty, r)$ (12) is non-zero and the fracture volume equals to the

$$V = \frac{16\sigma_y^\infty R^3}{3E'}. \tag{41}$$

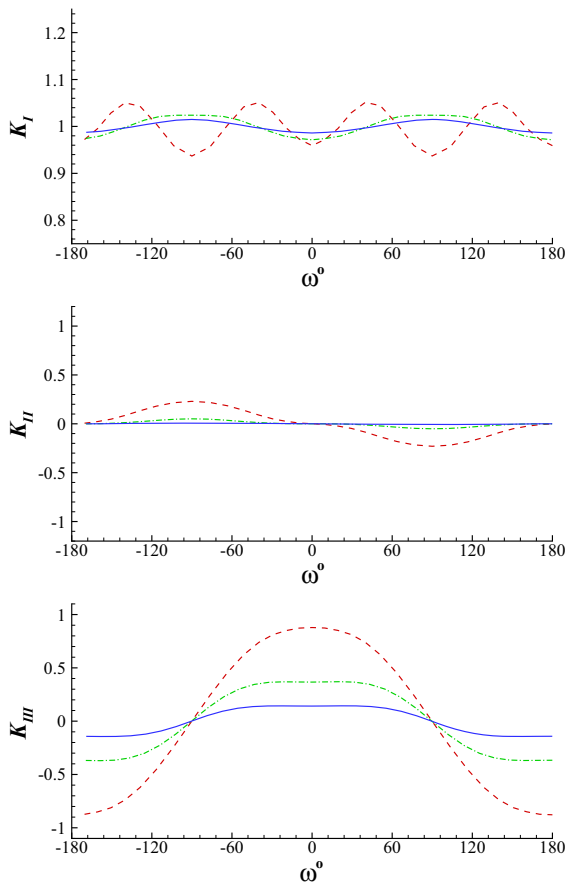


Fig. 20 SIFs along crack front with $\beta = 0.5$: step 2 (dashed); step 10 (dashed-dotted); step 30 (solid)

While the condition (40) is fulfilled, the increase of σ_y^∞ in (41) leads to the growth of V and the fracture radius R is constant. Because of the further σ_y^∞ increase, the condition

$$K_I > K_{Ic}, \tag{42}$$

is fulfilled. Then the equation

$$K_I \equiv 2\sigma_y^\infty \sqrt{\frac{R}{\pi}} = K_{Ic} \tag{43}$$

gives a new crack front position

$$R = \frac{\pi K_{Ic}^2}{4(\sigma_y^\infty)^2} \tag{44}$$

and its volume

$$V = \frac{\pi^3 K_{Ic}^6}{12E'(\sigma_y^\infty)^5}. \tag{45}$$

Let us examine the initial fracture described in the section 4.1, with $R = 1m$ in the elastic media with $E =$

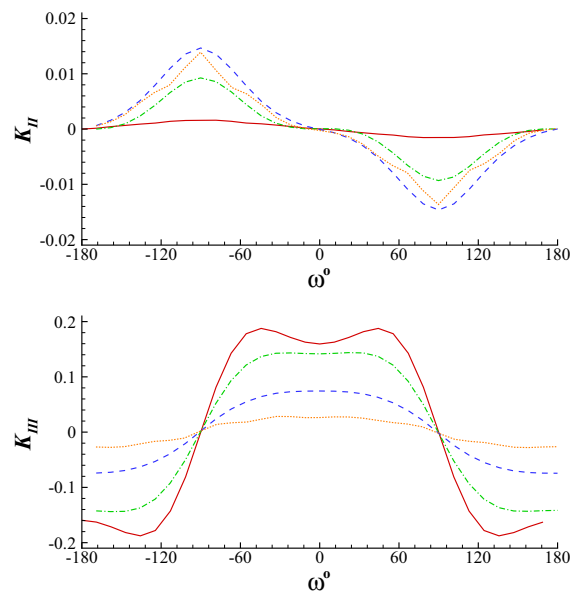


Fig. 21 SIFs along crack front at step 30: $\beta = 0$ (solid); $\beta = 0.5$ (dashed-dotted); $\beta = 0.8$ (dashed); $\beta = 0.9$ (dotted)

20 GPa, $\nu = 0.2$, $K_{Ic} = 3 \text{ MPa } \sqrt{m}$. Starting from the initial tension $\sigma_y^\infty = 1 \text{ MPa}$ fracture load will begin to rise consequently. After the fracture starts to grow, the tension σ_y^∞ and the fracture radius R are adjusted to fulfill the condition (44). Figure 22 compares the solution for the problem of fracture propagation in the case of unloaded media under tensile stress: the analytical solution obtained above for the case $\alpha = 0$ and the numerical solution obtained using the developed model.

In the case of non-zero initial fracture inclination angle α an equivalent quasi-static growth shown in Fig. 23 will be obtained. Results displayed there were obtained numerically using the described algorithm. The trajectories of fracture propagation with different inclination angles are shown in Fig. 24.

5.1.2 Loaded fracture in a compressed elastic media

In this section the other statement of quasi-static crack growth problem is considered. This statement is more appropriate for the simulation the simulation of hydraulic fracturing process than the previous one (section 5.1.1). The statement is shown in Fig. 25. There is a penny-shaped initial fracture of radius R in an inclined to axis Oz at an angle α plane. This can be either an isolated crack, or a crack that adjoins a wellbore of radius

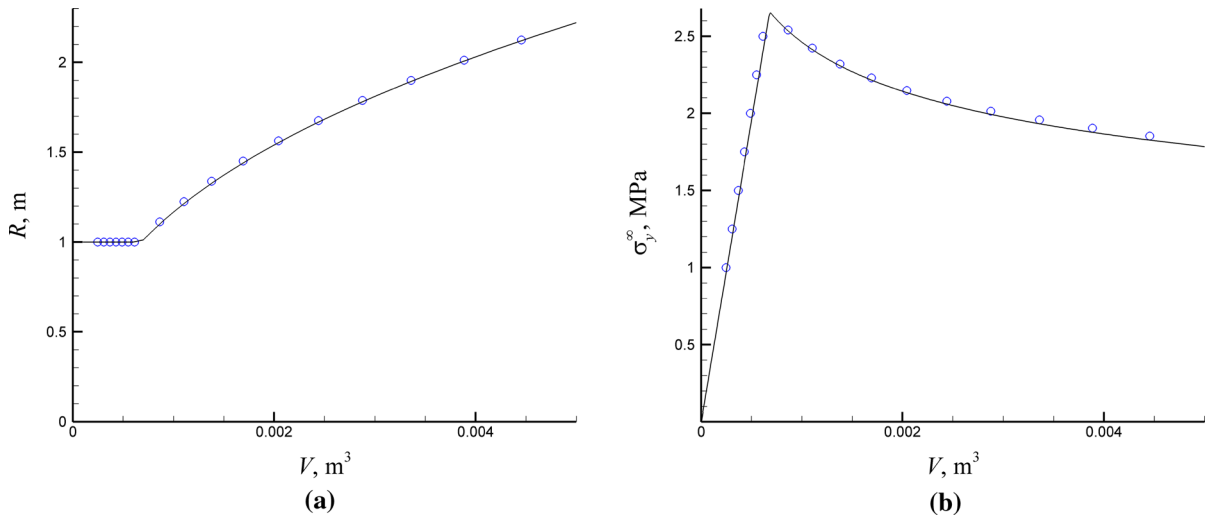


Fig. 22 Crack front radius R (a) and σ_y^∞ (b) as a functions of fracture volume V : analytical solution (solid line); numerical (circle)

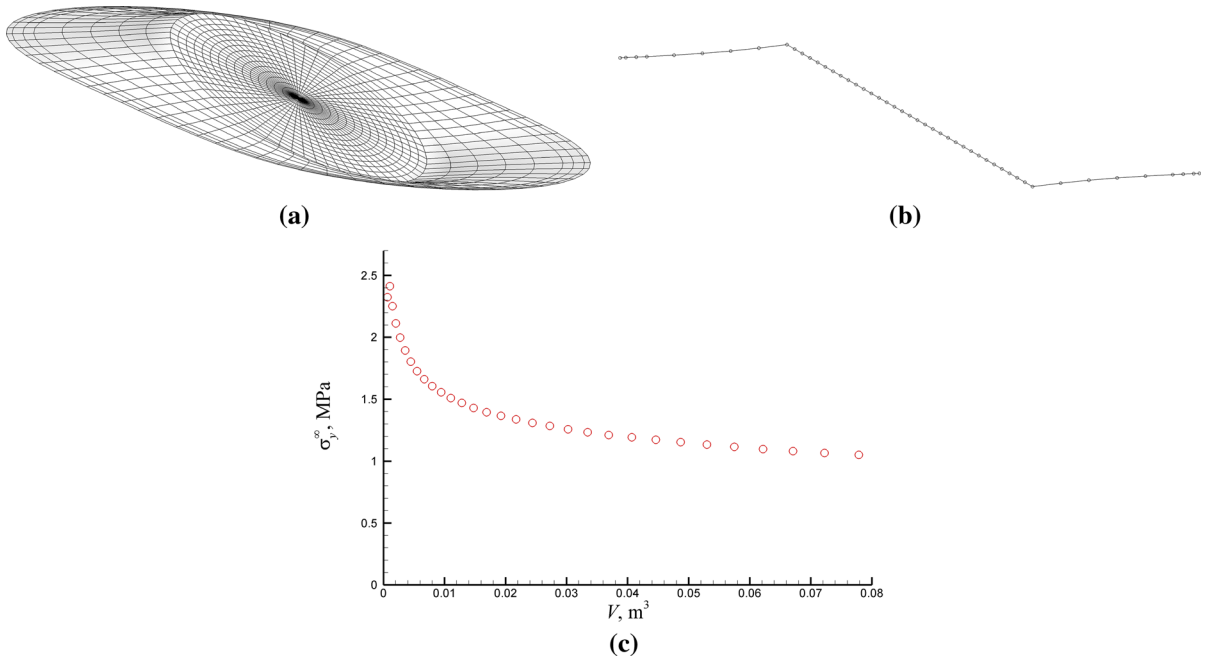


Fig. 23 Quasi-static propagation of an initial fracture inclined by $\alpha = 30^\circ$ in a media under a tensile stresses σ_y^∞ : **a** fracture shape after step 6; **b** fracture trajectory in section $z = 0$; **c** variation of σ_y^∞ and V during the crack growth

R_w and is perpendicular to this wellbore. The surrounding media is loaded at the infinity by compressing principal stresses $\sigma_x^\infty, \sigma_y^\infty, \sigma_z^\infty$, that have negative values. The wellbore and the initial fracture are loaded from the inside with pressure p . By adjusting the value p which is necessary for fracture propagation, the quasi-

static crack growth shown in Fig. 25 can be observed. The algorithm of the numerical solution of this problem and the analysis of the influence of wellbore presence towards fracture trajectories will be given thereafter.

The simulations were performed with the following parameter values: $E = 20$ GPa, $\nu = 0.2$, $K_{Ic} =$

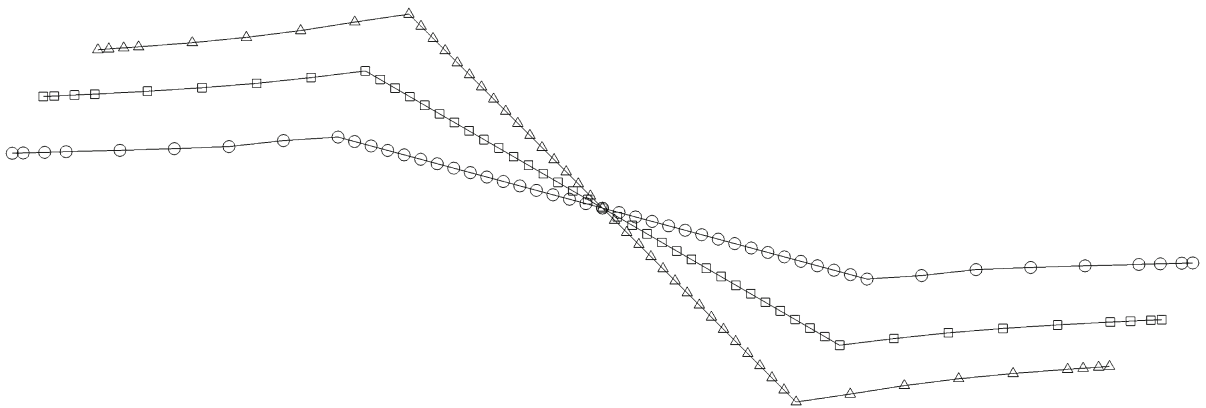


Fig. 24 Fracture trajectories: $\alpha = 15^\circ$ (circle), $\alpha = 30^\circ$ (square), $\alpha = 45^\circ$ (triangle)

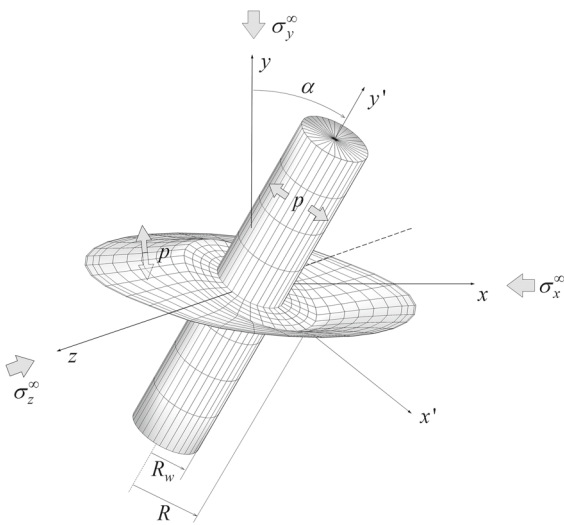


Fig. 25 Cavity and fracture loaded with pressure p in a media, which is compressed by a tensor σ^∞ on an infinite distance

$3 \text{ MPa} \sqrt{m}$, $R = 1 \text{ m}$, $R_w = 0.5 \text{ m}$, $\alpha = 30^\circ$, $\sigma_x^\infty = -16 \text{ MPa}$, $\sigma_y^\infty = -12 \text{ MPa}$; $\sigma_z^\infty = -16 \text{ MPa}$.

The analysis of fracture trajectory sensitivity towards the principal in situ stress, and the wellbore presence in the problem statement is shown in Fig. 26.

The isometric projections of fracture obtained during the quasi-static propagation with the fixed in situ stress $\sigma_x^\infty = \sigma_z^\infty = 16 \text{ MPa}$ and the varied in situ stress $\sigma_y^\infty = 8 \text{ MPa}$ (left) and 15.9 MPa (right) are shown in Fig. 27. Also, their trajectories in $z = 0$ plane are compared in this figure.

5.2 Viscous fluid crack growth

The fracture surface in 3D space and its piecewise planar representation are shown in Fig. 28. Through the boundary S^q the fracturing fluid is pumped from the wellbore to the crack. The boundary S^p is a fluid's front.

At each planar piece of fracture the lubrication approximation for a Newtonian fluid flow of viscosity μ between parallel plates, with distance W between each other, gives

$$\mathbf{q} = -\frac{W^3}{12\mu} \nabla p \tag{46}$$

where \mathbf{q} is the fluid flux.

The mass conservation equation can be written as follows

$$\frac{\partial W}{\partial t} + \nabla \cdot \mathbf{q} = 0. \tag{47}$$

From (46) - (47) it is possible to obtain the following equation for p :

$$\nabla(a \nabla p) = f, \tag{48}$$

where $a = \frac{W^3}{12\mu}$, $f = \frac{\partial W}{\partial t}$.

Boundary conditions for the equation (48) are the following:

$$p|_{S^p} = p_{pore} \tag{49}$$

and the inflow condition is

$$\int_{S^q} \mathbf{q} \cdot \mathbf{n}_q dS = Q_{in}, \tag{50}$$

where \mathbf{n}_q is the normal to the boundary S^q . In terms of pressure the latter condition (50) with consideration of

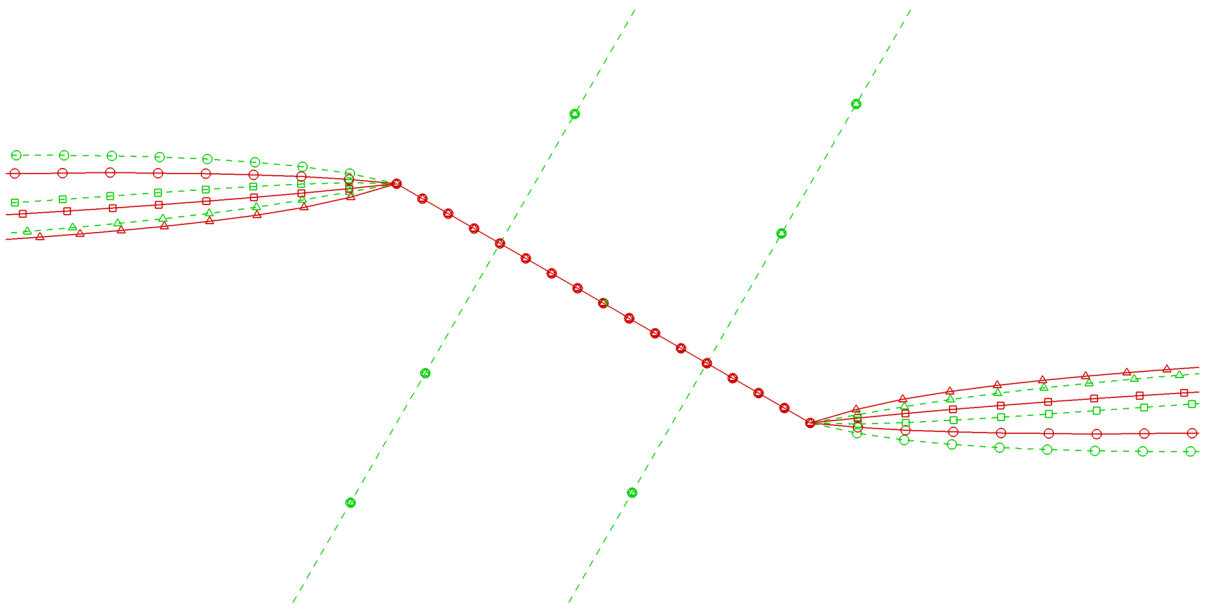


Fig. 26 Fracture trajectories in statements with a wellbore (*dashed line*) and without it (*solid*): $(\sigma_x^\infty; \sigma_y^\infty; \sigma_z^\infty) = -(4; 3; 4)$ MPa (*circle*), $-(8; 6; 8)$ MPa (*square*), $-(16; 12; 16)$ MPa (*triangle*)

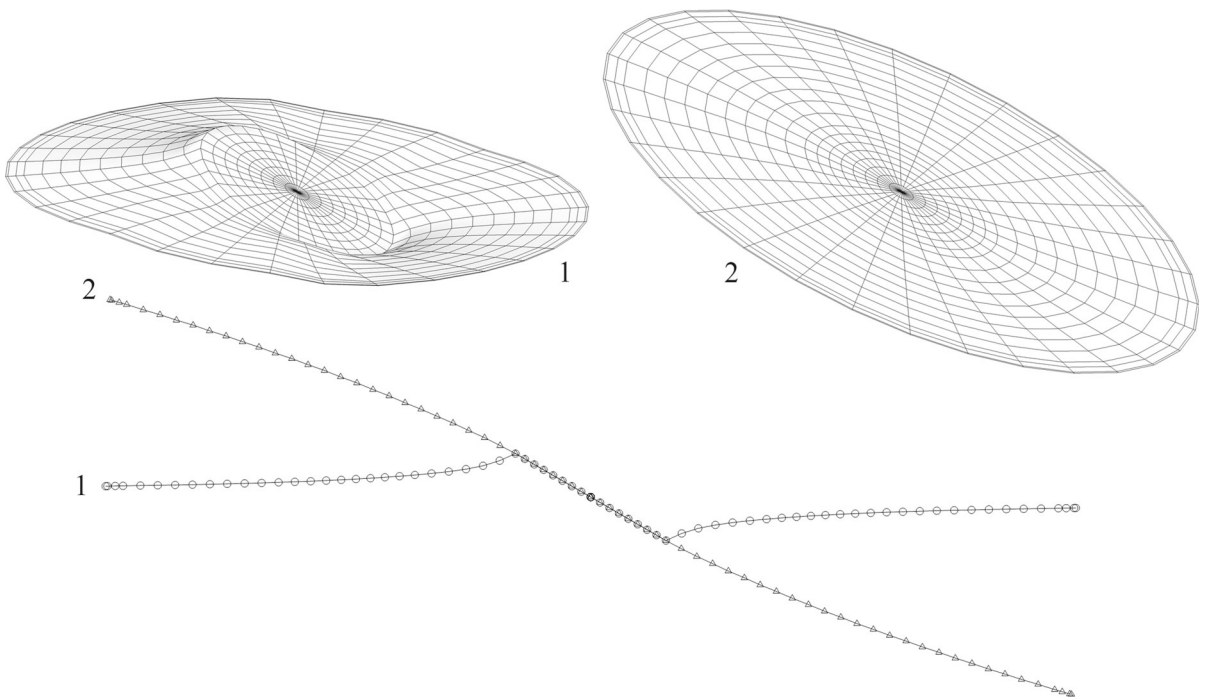


Fig. 27 Quasi-static fracture propagation: 1 $\sigma_y^\infty = 8$ MPa (*left*); 2 $\sigma_y^\infty = 15.9$ MPa (*right*); fracture trajectories in section $z = 0$ (*down*)

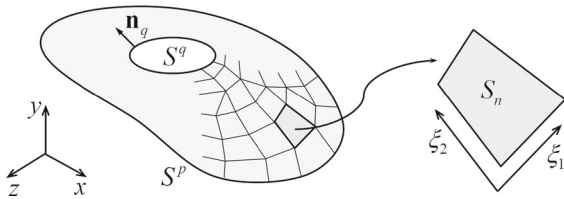


Fig. 28 Fracture surface in 3D space and its piecewise planar representation

(46) is rewritten as

$$\int_{S^q} a \frac{\partial p}{\partial n} dS = -Q_{in}. \tag{51}$$

It is assumed that the fluid front moves with the same speed \mathbf{v}_f , as the fluid particles $\mathbf{v}(\mathbf{x})$ at the front (Stefan condition) do

$$\mathbf{v}_f(\mathbf{x}) = \mathbf{v}(\mathbf{x}) = \mathbf{q}(\mathbf{x})/W(\mathbf{x}), \quad \mathbf{x} \in S^p. \tag{52}$$

The algorithm of the condition (51) implementation assumes two variants of crack orientation: transversal and longitudinal (Fig. 29).

The inflow rate distribution should be set on the boundary S^q . In the case of transversal crack the flow domain is extended with an imaginary domain in the wellbore (Fig. 30). The boundary condition for the volumetric injection rate Q_{in} (51) is set at the wellbore center \mathbf{x}_{in} . The condition at the injection point \mathbf{x}_{in} is incorporated directly into the continuity equation. To do so, the equation (47) is re-written as

$$\frac{\partial W}{\partial t} + \nabla \cdot \mathbf{q} - \delta(\mathbf{x} - \mathbf{x}_{in})Q_{in} = 0, \tag{53}$$

and the equation (48) is re-written as

$$\nabla(a\nabla p) = f - \delta(\mathbf{x})Q_{in}. \tag{54}$$

The crack width in the imaginary domain is set $W = 10^5 m$. According to the equation (48) this

value provides constant pressure in this domain. Therefore, the distribution of the inflow rate along the S^q is defined during the computation with the assumption that the pressure along this boundary is constant $p(\mathbf{x}) = const, \mathbf{x} \in S^p$.

According to the FEM the equation (54) is re-written in weak formulation

$$\int_{S_n} \nabla(a\nabla p)\omega dS = \int_{S_n} (f - Q_{in}\delta(\mathbf{x}))\omega dS, \tag{55}$$

where ω is a test function. After that, the solution is represented in the form

$$p(\xi_1, \xi_2) = \sum_{i=1}^M p^i \phi_i(\xi_1, \xi_2), \tag{56}$$

the system of equations for each element is written as

$$K_{ij}p^i = Q_j + F_j + Q_{in}\tilde{\delta}(\mathbf{x}), \tag{57}$$

where

$$K_{ij} = \iint_{S_n} a \nabla \phi_i \cdot \nabla \phi_j |J| d\xi_1 d\xi_2,$$

$$Q_j = \int_{\partial S_n} a \frac{\partial p}{\partial n} \phi_j dG, \tag{58}$$

$$F_j = - \iint_{S_n} f \phi_j |J| d\xi_1 d\xi_2,$$

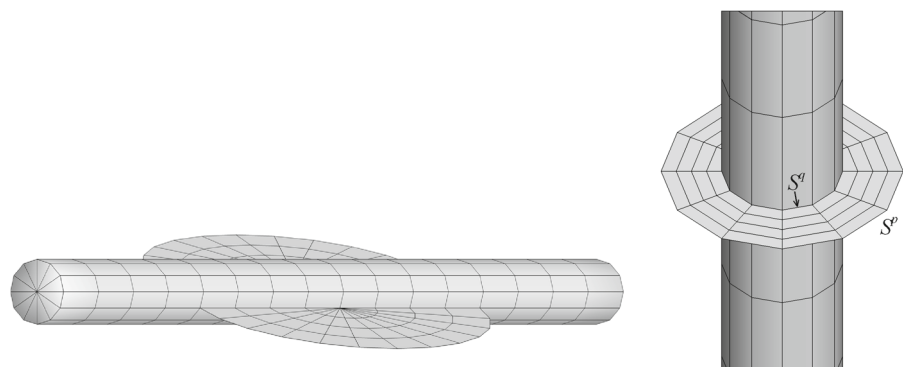
$\tilde{\delta}(\mathbf{x}) = 1$ at $\mathbf{x} = \mathbf{x}_{in}$, and $\tilde{\delta}(\mathbf{x}) = 0$ at $\mathbf{x} \neq \mathbf{x}_{in}$.

Finally, the united system of linear equations is obtained by assembling element stiffness matrices to global stiffness matrix

$$\mathbf{Kp} = \mathbf{Q} + \mathbf{F} + \mathbf{Q}_{in}. \tag{59}$$

There, the boundary equation for Q_{in} is taken into account in the right part of \mathbf{Q}_{in} .

Fig. 29 Schemes of longitudinal (left) and transversal (right) cracks



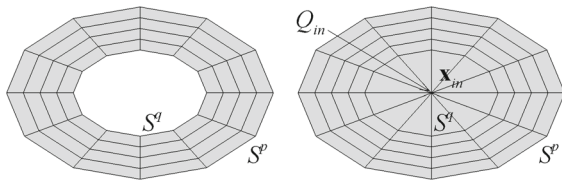


Fig. 30 Inflow rate for the transversal crack: initial fracture inlet boundary (left), inlet boundary modified with inflow addition (right)

The features of a longitudinal crack are the following: there are two fracture wings, the distribution of the inflow rate among them is unknown, and there is a boundary part S^q , with no inflow rate on it. Such boundary part appears for example when the system contains a casing.

As well as in the case of transversal crack, the imaginary flow domain is applied here. It connects boundaries with non-zero inflow rate and a point \mathbf{x}_{in} where the total volumetric inflow rate is set. As a result of the system (59) solution, the inflow rate on the part of the boundary S_0^q is equal to zero, its distribution along the boundaries $S_1^q \cup S_2^q$ is calculated so that the pressure along this boundary is constant, and the total inflow rate equals to the volumetric inflow rate (Fig. 31).

6 Results of fracture propagation simulations

Crack propagation algorithm is discussed in the Appendix.

6.1 1D verification

6.1.1 Radial hydraulic fracture propagating

To verify the model, the numerical simulations of a plane-radial fracture propagation under a viscous fluid loading and a comparison with the previous results obtained using the one-dimensional model (Esipov et al. 2014) were done. There, the one-dimensional model of material deformation under an axially symmetric pressure distribution is described by the relation

$$W(r) = \frac{8}{\pi E'} \int_r^R \left(\int_0^\xi \frac{p_{net}(\xi)\xi}{\sqrt{\xi^2 - \xi^2} \sqrt{\xi^2 - r^2}} d\xi \right) d\xi, \tag{60}$$

where $R = R(t)$ is the crack front position defined from

$$K_I = \frac{2}{\sqrt{\pi R}} \int_0^R \frac{p_{net}(\xi)\xi}{\sqrt{R^2 - \xi^2}} d\xi = K_{Ic}. \tag{61}$$

The net pressure $p_{net} = p - \sigma_{min}$ is defined as the pressure in the crack minus stress σ_{min} against which it opens.

The fluid flow is described by the continuity equation

$$\frac{\partial W}{\partial t} + \frac{1}{r} \frac{\partial(r Wu)}{\partial r} + Q_L(r, t) = 0 \tag{62}$$

and the momentum equation

$$\frac{\partial p_{net}}{\partial r} = -\frac{12\mu}{W^2} u. \tag{63}$$

The fluid leak-off to the rock Q_L is described by the Carter law (Esipov et al. 2014).

The fluid flow equations (62) and (63) are completed with the boundary condition in the wellbore of radius R_w

$$2\pi R_w Wu = Q_{in}. \tag{64}$$

The lag between the fluid front R_f and the fracture front R is assumed

$$R - R_f > 0. \tag{65}$$

The position of the fluid front R_f is defined from the equation

$$Q(R_f, t) = 0, \tag{66}$$

and the boundary condition for (62) and (63) at the fluid front R_f takes the form of

$$p_{net}(R_f, t) = -\sigma_{min}. \tag{67}$$

Note that the net pressure p_{net} in the area between the fluid front and the fracture tip is also considered equal to the $-\sigma_{min}$.

Initial data is

$$\begin{aligned} R(0) &= R_0, & R_f(0) &= R_0, \\ W(r, 0) &= W_0, & R_w \leq r \leq R_0. \end{aligned} \tag{68}$$

The problem (60)–(68) is solved for the parameters $E = 20$ GPa, $\nu = 0.2$, $K_{Ic} = 3$ MPa $\sqrt{\text{m}}$, $\sigma_{min} = 3$ MPa, $\mu = 1000$ Pa s, $Q_{in} = 16$ cm³/s, $Q_L = 0$. The initial fracture radius is $R_0 = 1$ m, the wellbore radius $R_w = 0.5$ m. The same problem is solved using the 3D fracture propagation model with BEM/DM, proposed in the present paper. In this case the wellbore

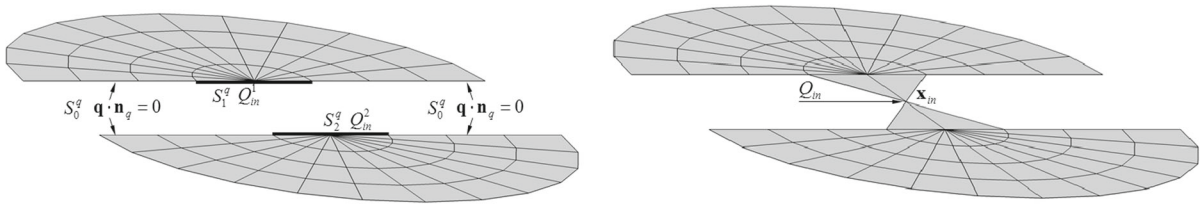


Fig. 31 Inflow rate for the longitudinal crack: structure of boundary S^q (above); imaginary flow domain (below)

Fig. 32 The wellbore and crack surface representation at various crack growth steps (left is the wellbore with the initial fracture)

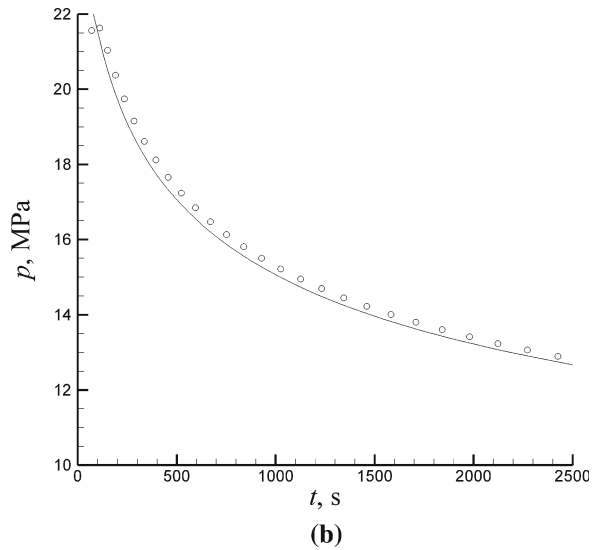
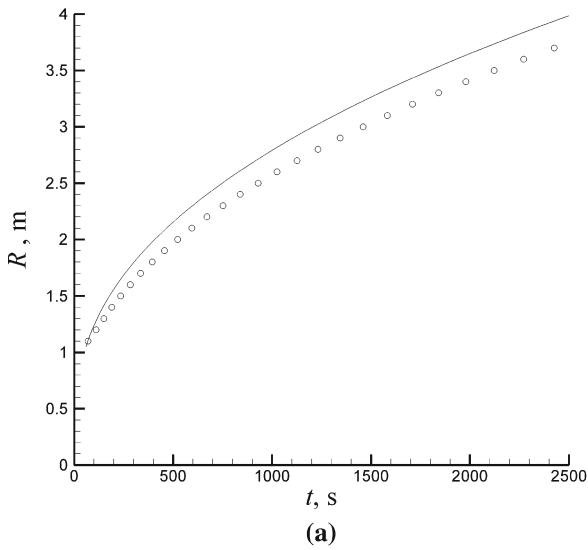
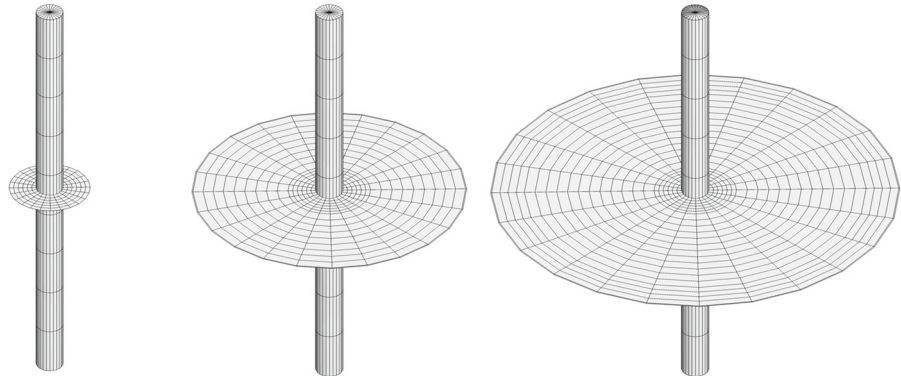


Fig. 33 Radius of the crack R (a) and injection pressure p (b) as functions of the time: one-dimensional problem (60)–(68) (solid line); three-dimensional model (circle)

cavity of radius $R_w = 0.5$ m with the initial fracture of radius $R_0 = 1$ m were added to the problem statement (Fig. 32). It is assumed that the fracture propagation criterion (61) is fulfilled from the very beginning of the problem solution. It is achieved by adjusting the

time step value Δt so that the volume of pumped fluid is enough to produce the pressure of propagation. The comparison between 1D problem solution (60)–(68) and one obtained using the developed model is shown in Fig. 33.

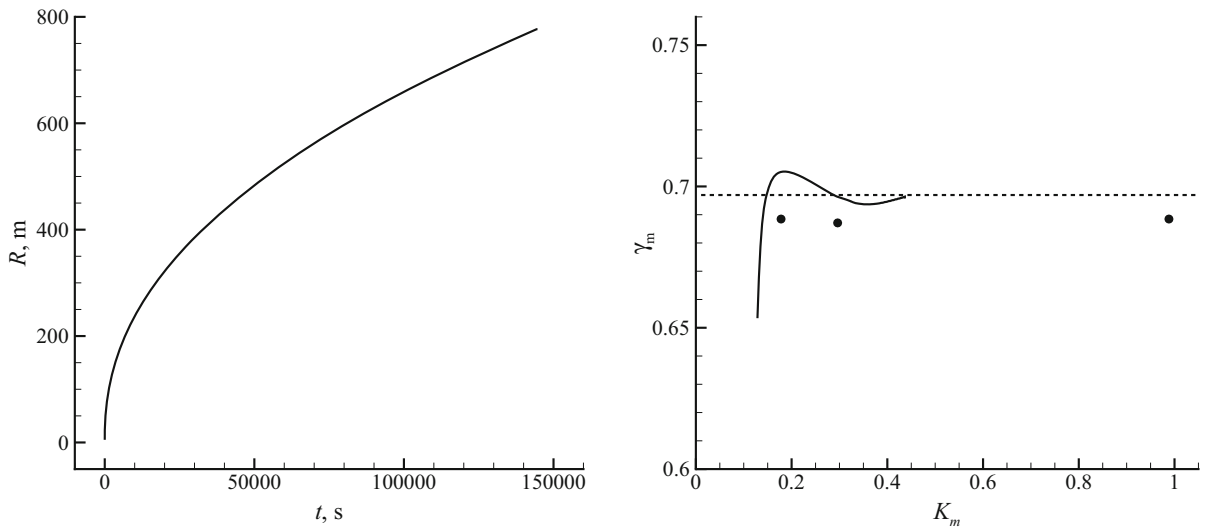


Fig. 34 Dimensional (*left*) and scaled (*right*) fracture radius versus time: *solid* 3D model; *dashed* analytical solution (Savitski and Detournay 2002); *circle* numerical solution (Savitski and Detournay 2002)

6.1.2 Verification against analytical solution for viscous propagation regime

In Savitski and Detournay (2002) the authors introduce two regimes of radial hydraulic fracture propagation: viscous and toughness regimes. The toughness-dominated regime is characterized by the high pressure gradient near the fluid front. This gradient can be described accurately under the assumption that the lag between the fracture front and the fluid front is negligibly small. Under this assumption, the pressure at the fracture front is singular and special solution procedures are used to calculate it. In our 3D model the lag is taken into account and it requires a lot of computational resources to describe it precisely. So the only viscous propagation regime that has been simulated and compared with the solutions is presented in Savitski and Detournay (2002).

To verify the coupled version of the proposed 3D model a numerical simulation of radial hydraulic fracture propagating in viscous regime has been performed and the results obtained were compared to the analytical solution from Savitski and Detournay (2002). For the comparison, a borehole with radius $R_w = 0.02$ m and a penny-shaped initial fracture with radius $R_w = 0.079$ m that are placed in an elastic media which is strained at the infinity by the stress $\sigma_x^\infty = \sigma_y^\infty = \sigma_z^\infty = 41.4$ MPa are considered. The param-

eters of the media are the following: Young modulus $E = 38.8$ GPa, Poisson’s coefficient $\nu = 0.15$ and fracture toughness $K_{Ic} = 1$ MPa \sqrt{m} . The borehole’s axis coincides with the axis $y(\alpha = 0)$. The fluid with viscosity $\mu = 0.08$ Pa \cdot s and rate $Q_{in} = 0.053$ m³/s is pumped into the borehole.

The fracture radius R obtained as a function of time t using the 3D model is shown in Fig. 34. Also, the numerical and the analytical (Savitski and Detournay 2002) dimensionless crack radii γ_m as functions of dimensionless toughness K_m are shown in Fig. 34. The dimensionless fracture radius γ_m and the dimensionless toughness K_m which can be identified with an evolution parameter (i.e. time) are calculated using the formulae given in Savitski and Detournay (2002)

$$\gamma_m = R(t)/L(t), \quad L(t) = \left(\frac{E' Q_{in}^3 t^4}{12\mu} \right)^{1/9}, \quad (69)$$

$$K_m = 4K_{Ic} \left(\frac{2}{\pi} \right)^{1/2} \left(\frac{t^2}{(12\mu)^5 Q_{in}^3 E'^{13}} \right)^{1/18}. \quad (70)$$

Figure 35 shows the distributions of dimensionless width

$$\Omega_m = \frac{w}{\varepsilon L}, \quad \varepsilon = \left(\frac{12\mu}{E't} \right)^{1/3} \quad (71)$$

and dimensionless pressure

$$\Pi_m = \frac{p}{E'\varepsilon} \quad (72)$$

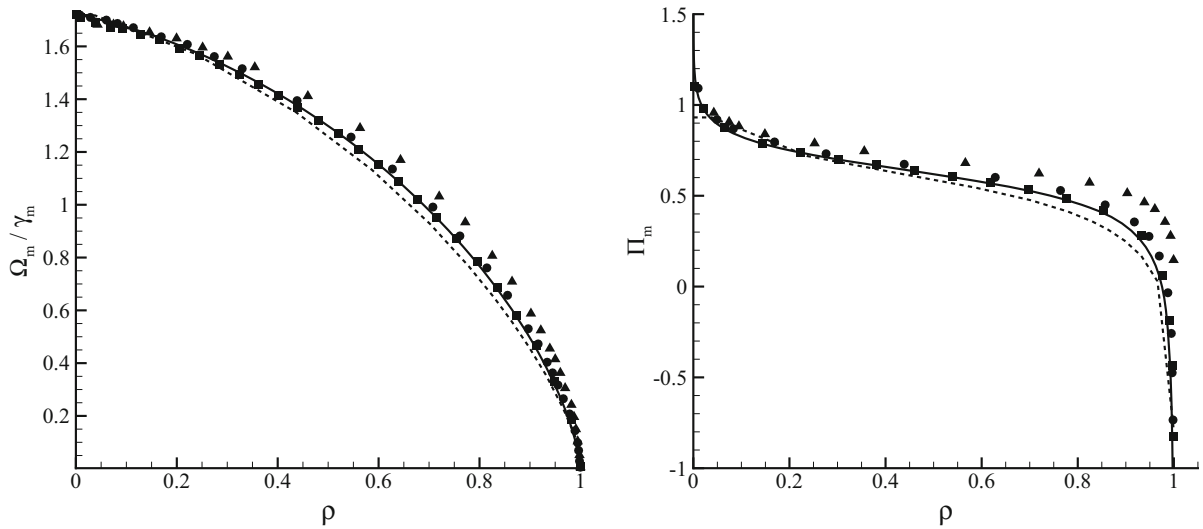


Fig. 35 Scaled fracture width (*left*) and pressure (*right*) along the fracture radius: *dashed* 3D model $K_m = 0.15$; *solid* 3D model $K_m = 0.45$; *square* analytical solution (Savitski and

Detournay 2002) $K_m = 0$; *circle* numerical solution (Savitski and Detournay 2002) $K_m = 0.15$; *triangle* numerical solution (Savitski and Detournay 2002) $K_m = 1.5$

along the dimensionless radius $\rho = r/R$ at the time moments $t = 10$ s, $t = 40$ h, which correspond to the dimensionless toughness $K_m = 0.15$ and $K_m = 0.45$. Also, there are shown the distributions of dimensionless width and pressure calculated analytically and using the Loramec code (Desroches and Thiercelin 1993; Carbonell et al. 1999), that are given in Savitski and Detournay (2002) for the values of dimensionless time $K_m = 0.15$ and $K_m = 1.5$. The value $K_m = 1.5$ corresponds to the physical time $t = 300$ years, which cannot be calculated using the present 3D model. Therefore the dimensionless toughness $K_m = 0.45$ corresponding to $t = 40$ h has been chosen instead of it.

The present 3D model is designed for the calculation of initial stage of hydraulic fracturing during which the fracture remains in viscous regime of propagation. Fig 35 shows that at this regime the errors of calculation of width and pressure do not exceed 10%.

6.2 3D verification of model

The developed 3D model was applied to the simulation of fracture propagation under conditions of Chang et al. (2014) where hydraulic fracturing laboratory tests have been performed with the objective to study multiple initiations of hydraulic fractures at multiple notches

placed in the wellbore (see Fig. 36). The key point of the experimental investigation (Chang et al. 2014) was to obtain the conditions of two possible scenarios: one longitudinal fracture propagation or multiple transversal fracture propagation. The simulation of fracture initiation is described in Aidagulov et al. (2015) and here the fracture propagation is simulated. The key point of the numerical investigation was to show that the model is able to predict the fracture propagation direction correctly.

6.2.1 Longitudinal fracture propagation

In the Tests 1 and 2 (Chang et al. 2014) the notch depth varies from 0.125 to 0.375 of wellbore diameter. The longitudinal fracture initiates at the wellbore wall in the area between the notches. The simulations of fracture propagation have been performed in quasistatic statement. Considering this case allows to skip the part of numerical algorithm where the hydrodynamics-elasticity problem is solved. It is assumed that at each timestep the fluid pressure within the wellbore, notches and the fracture is the same. This reduces computational time and eventually allows using a finer computational mesh and a smaller fracture increment. For the same purpose, the computational domain was infinite, though the blocks used in the experiments were finite. However, they were large enough to allow such

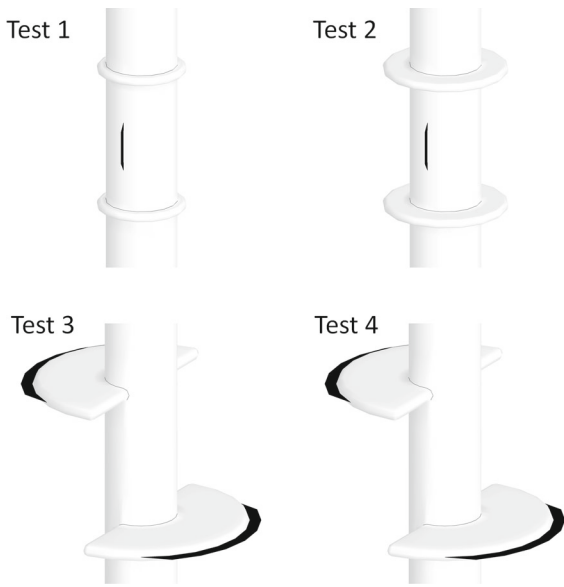


Fig. 36 Fracture initiation patterns observed in simulations of the tests (Chang et al. 2014)

I rock fracture toughness was $K_{Ic} = 1 \text{ MPa}\sqrt{\text{m}}$, and the tensile strength was $\sigma_c = 5.2 \text{ MPa}$.

In the simulation the fracture propagates along the wellbore up and down “walking around” the notches. The injection pressure obtained in the simulation varies within the interval of $p = 25 \div 30 \text{ MPa}$ that is lower than the one observed in the experiment because of the the absence of pressure gradient inside the fracture. The fracture propagation speed is very high and notches are overcome in less than one second.

In order to simulate the hydraulic fracture “walking around” the notches, one has to use a small fracture increment parameter and a very fine mesh. The authors consider this as one of the main obstacles towards the simulation of this fracture-walk-around in a fully coupled case of viscous fluid. Therefore, the fully coupled model was not applied to this case.

simplification. Figure 37 shows fracture shape for various time moments. Disregard the viscosity, the fracture propagation was simulated for the geometry and the parameters corresponding to the Test 2. The mode

6.2.2 Transverse fracture propagation

In Tests 3 and 4 described in Chang et al. (2014) transverse fractures initiate and grow at the edges of the notches. As long as both tests have an equal geometry and similar far field stresses are applied, the investigation has been focused on the Test 3 only. The surface

Fig. 37 Snapshots of fracture propagation at various time moments

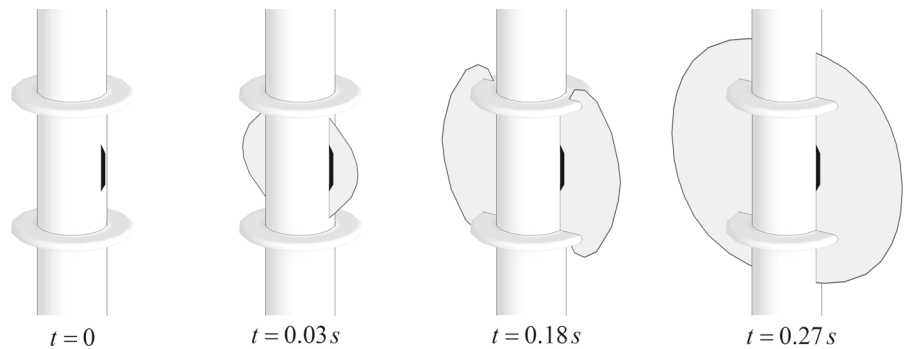
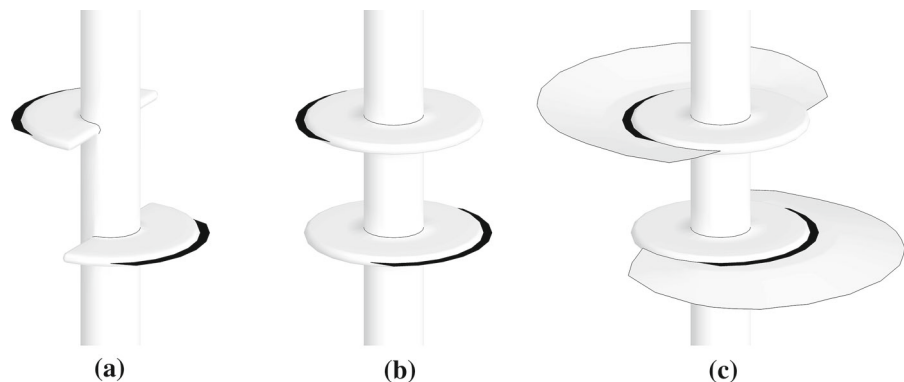


Fig. 38 Geometry and incipient fractures for the Test 3: lab Test 3 geometry and incipient fractures (a); simplified statement (b); crack propagation at $t = 0.25 \text{ s}$ (c)



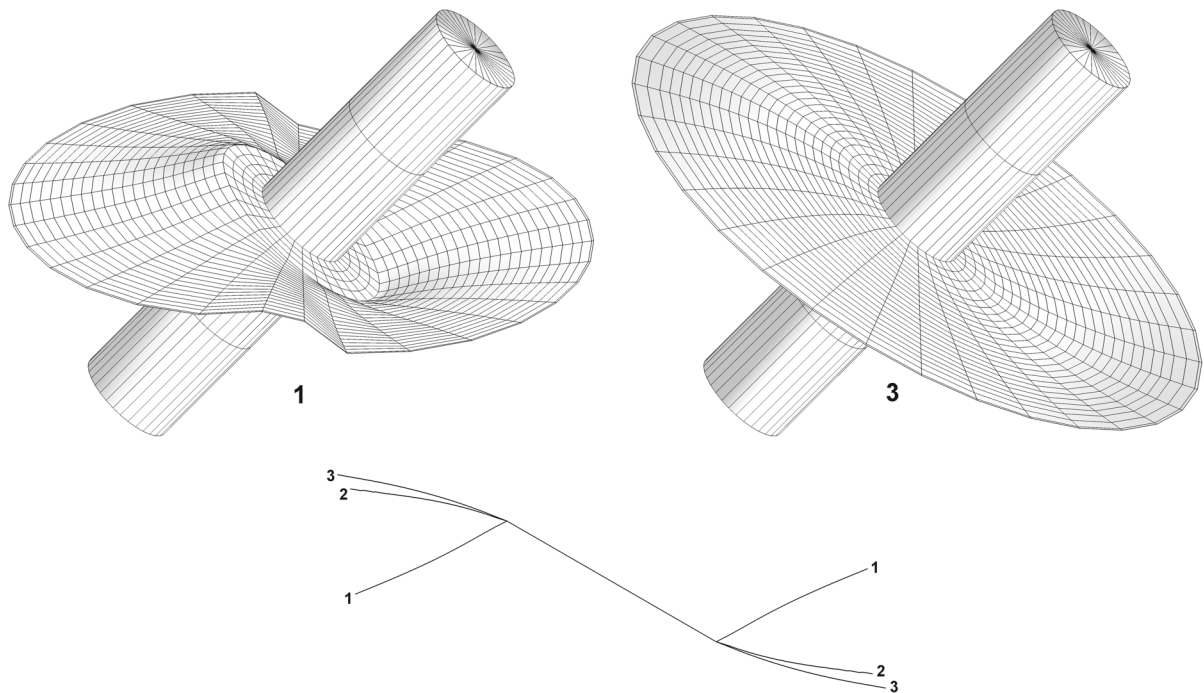


Fig. 39 Fracture trajectories and their cross-sections: 1 quasistatic approach; 2 viscous fluid approach $\mu = 100 \text{ Pa} \cdot \text{s}$; 3 viscous fluid approach $\mu = 1000 \text{ Pa} \cdot \text{s}$

geometry at the corner between the semicircular notch and the wellbore (see Fig. 38a) is complex. Very small fracture increment step is needed to simulate the fracture propagation along such surface. Otherwise, it is difficult to obtain the convergence of iteration algorithms. To avoid this difficulty the simplified computational domain has been considered (see Fig. 38b). It consists of the wellbore, two circular notches and two incipient fractures obtained by solving the initiation problem with the original computational domain (Fig. 38a) (Aidagulov et al. 2015). The parameters of the problem are: $E = 20 \text{ GPa}$, $\nu = 0.2$, $\sigma_x^\infty = 20.7 \text{ MPa}$, $\sigma_y^\infty = 15.5 \text{ MPa}$, $\sigma_z^\infty = 24.1 \text{ MPa}$, $\sigma_c = 5.2 \text{ MPa}$, $K_{Ic} = 1 \text{ MPa}\sqrt{\text{m}}$, $Q_{in} = 0.5 \text{ cm}^3/\text{s}$, notch depth is equal to the wellbore diameter.

The initiated fracture propagates with a high speed along the notch edge. Figure 38, c shows the fracture geometry at the time moment $t = 0.25 \text{ s}$ after the fracture started to propagate. Therefore, the form of the incipient fracture and its position are not important but its orientation affects the propagation process only.

6.3 3D viscous fluid crack growth

6.3.1 Comparison of quasistatic and viscous fluid approaches

Here, the simulation of a transverse fracture propagation is shown. A wellbore with the transverse fracture is placed in a rock with Young modulus $E = 20 \text{ GPa}$, Poisson's ratio $\nu = 0.2$ and fracture toughness $K_{Ic} = 3 \text{ MPa}\sqrt{\text{m}}$. The rock is loaded by vertical $\sigma_y^\infty = 12 \text{ MPa}$ and two horizontal $\sigma_x^\infty = 16 \text{ MPa}$ and $\sigma_z^\infty = 16 \text{ MPa}$ stresses. The wellbore height and radius are $H = 5 \text{ m}$, $R_w = 0.5 \text{ m}$. The incipient fracture radius is $R = 1 \text{ m}$. The wellbore is inclined against the σ_y^∞ direction at an angle $\alpha = 45^\circ$ as it shown in Fig. 25. A fluid with viscosity μ is pumped into the wellbore with rate $Q_{in} = 1 \cdot 10^{-3} \text{ m}^3/\text{s}$. The fracture propagates and tries to reorient into the plane orthogonal to σ_y^∞ .

Two approaches are used for the simulation of fracture propagation. The quasistatic approach does not account the fluid viscosity. The viscous fluid approach

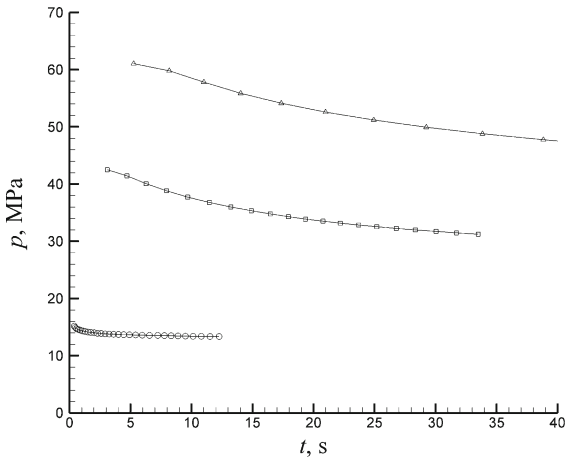


Fig. 40 Time dependence of fracture pressure: quasi-static model (circle); viscous fluid model with $\mu = 100 \text{ Pa} \cdot \text{s}$ (square) and with $\mu = 1000 \text{ Pa} \cdot \text{s}$ (triangle)

is applied with two values of fluid viscosity $\mu = 100$ and $1000 \text{ Pa} \cdot \text{s}$.

The 3D fracture trajectories and their cross-sections calculated using the quasistatic and the viscous fluid approaches are shown in Fig 39. In Fig. 40 the time dependence of fracture pressure is shown for the quasi-static and the viscous fluid models.

6.3.2 Longitudinal fracture propagation

The problem of longitudinal fracture propagation in a radially compressed media $\sigma_x^\infty = \sigma_y^\infty = \sigma_z^\infty = 16 \text{ MPa}$ with an elastic characteristics $E = 20 \text{ GPa}$, $\nu = 0.2$, $K_{Ic} = 3 \text{ MPa} \sqrt{\text{m}}$ (Fig. 41) is solved. The initial fracture has transversal size of 0.2 m and longitudinal size of 0.5 m , the wellbore radius is $R_w =$

Fig. 41 Longitudinal fracture propagation: 1 initial fracture at $t = 0$; 2 fracture at $t = 79\text{s}$; 3 $t = 378\text{s}$; 4 width of fracture's left wing at moment 3, magnified by 200

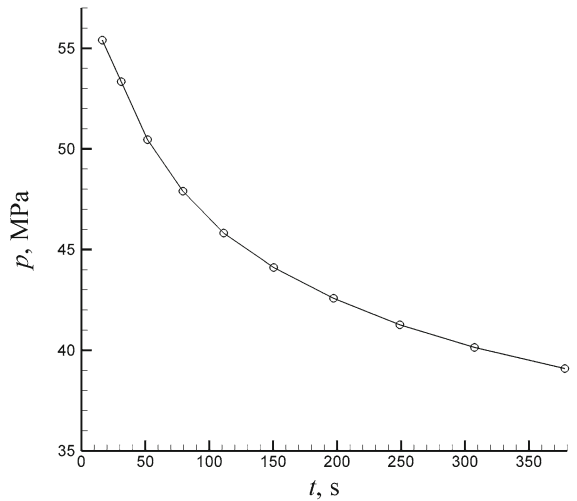
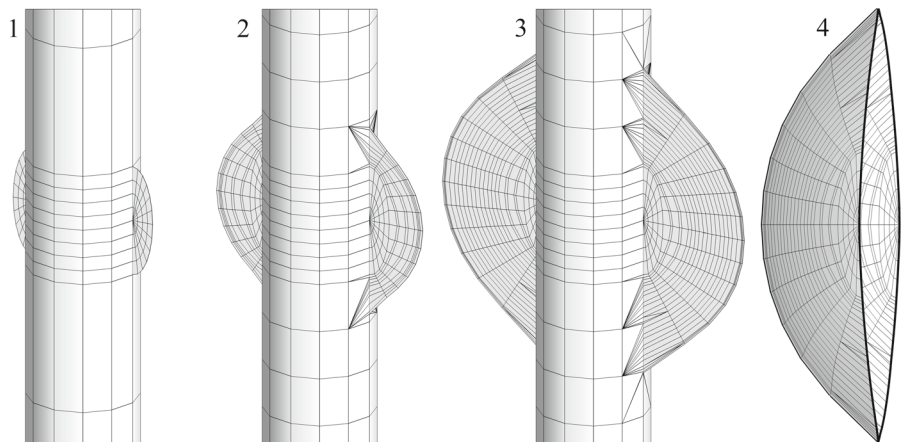


Fig. 42 Longitudinal fracture time-dependence of pressure in a pumping source

0.5 m . The fracture propagation is caused by the injection of a viscous fluid $\mu = 1000 \text{ Pa} \cdot \text{s}$ with discharge $Q_{in} = 10^{-5} \text{ m}^3/\text{s}$. The evolution of the fracture in time and the shape of the fracture at the last step of propagation are shown in Fig. 41. Figure 42 shows the relation between the fracture pressure and the time. The time is calculated as $t = V/Q_{in}$, where V is the volume of the fracture.

7 Conclusions

1. The conception of the 3D non-planar model of fracture propagation in elastic media and the numerical algorithm for its implementation are proposed.

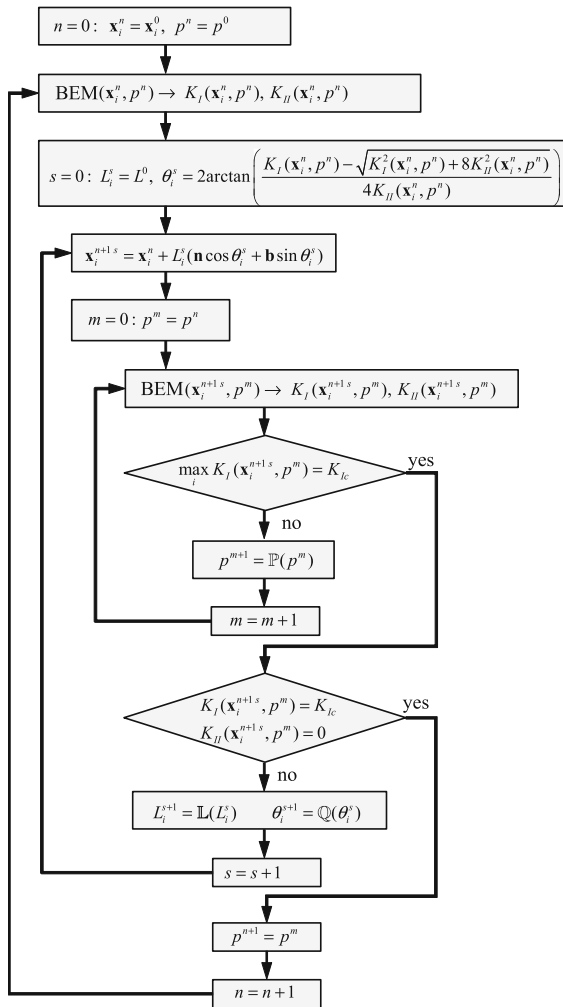


Fig. 43 Flow-chart of the quasi-static crack growth algorithm

2. The conception combines models of main connected problems that affect one another: stress-strain state, fracture loading, destruction of material, and fracture propagation.
3. The main advantage of the proposed conception is the possibility of using various models in every sub-problem without the necessity to rebuild the whole algorithm, which allows advancing from simple models to complex easily.
4. The first version of the model that combines the sub-models of elastic equilibrium, the Newtonian fluid flow, and the fracture propagation and direction criterion derived from the linear brittle fracture mechanics is implemented.

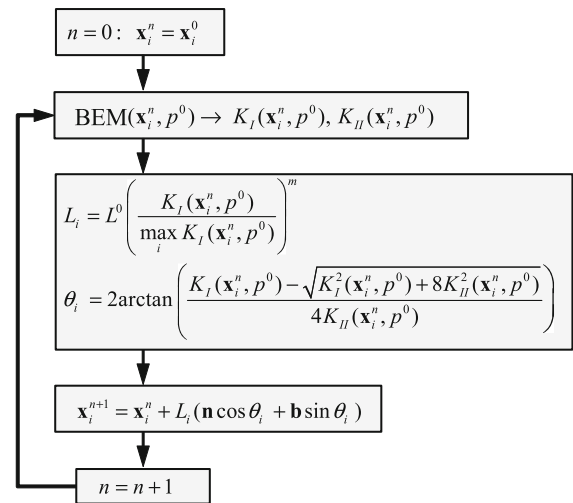


Fig. 44 Flow-chart of the fatigue crack growth algorithm

5. The verification of the model and the sensitivity analysis of solution to physical and numerical parameters is performed. It is shown that the results obtained are reliable.
6. In the next version of the model the approximation of a fracture with a finite width notch will be replaced by an infinitely thin fracture surface, which will be calculated together with a cavity by the DBEM; the algorithms of SIFs calculations will become more precise; the Newtonian fluid model will be replaced by a non-Newtonian one; the 3D model will be validated by experiments.

Acknowledgments Authors gratefully acknowledge the financial support of this research by the Russian Scientific Fund under grant number 14-11-00234.

Appendix

Crack propagation algorithm

Quasi-static crack growth

Let us consider the initial fracture with the front defined by vertices $x_i^0, i = 1, \dots, N_{fr}$. The case of an unloaded fracture in a stretched media and the case of a loaded fracture in a compressed media are combined in the algorithm by a generalized loading pressure p . A step-by-step fracture propagation is indicated with the superscript n . The general scheme of fracture prop-

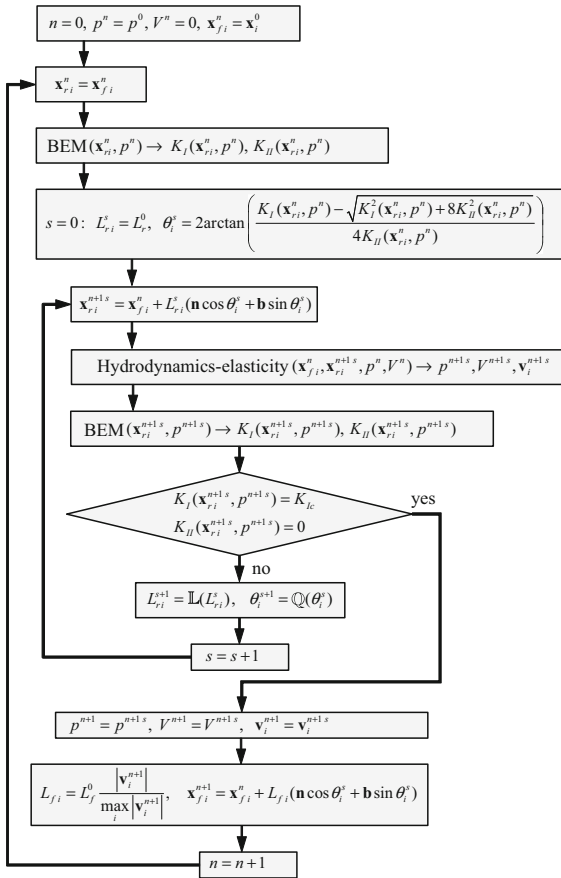


Fig. 45 Flow chart of dynamic fracture growth algorithm, derived viscous fluid flow

agation algorithm is displayed in Fig. 43. The iterative process

$$p^{m+1} = \mathbb{P}(p^m) \tag{73}$$

is introduced to achieve the fulfillment of the condition

$$\max_i K_I(x_i^{n+1,s}, p^m) = K_{Ic}. \tag{74}$$

The iterations

$$L_i^{s+1} = \mathbb{L}(L_i^s), \quad \theta_i^{s+1} = \mathbb{Q}(\theta_i^s) \tag{75}$$

provide the fulfillment of conditions

$$K_I(x_i^{n+1,s}, p^m) = K_{Ic}, \quad K_{II}(x_i^{n+1,s}, p^m) = 0 \tag{76}$$

at each vertex of the crack front at propagation step $n + 1$. The iterative schemes (73) and (75) are based on the methods of solving equations (74) and (76) respectively. The criteria (19) and (17) are implemented iteratively with the desired accuracy, at each vertex of the crack front, at every step of propagation algorithm

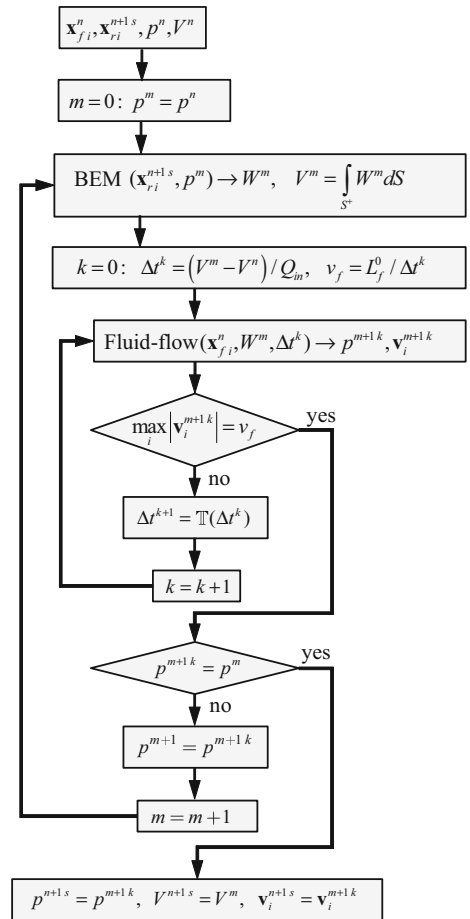


Fig. 46 Flow chart of the algorithm for hydrodynamics-elasticity problem solution

shown in Fig. 43. If the scaling law of crack incrimination is taken as a propagation criterion, and the direction of propagation is defined by the formula (16) itself, then the algorithm becomes essentially simpler (Fig. 44). The crack trajectories calculated using the algorithms in Fig. 43 and Fig. 44 are compared in the section 4.2.2 “Fatigue crack growth under cyclic loading – scaling law for crack front increment”.

Viscous fluid crack growth

Let the fracture be loaded by the pressure of viscous flow. The fluid front (labeled with its vertices $x_{f,i}^n$), the fracture front with vertices $x_{r,i}^n$, and the lag between fluid and fracture front $L_{r,i}$ are included into the algorithm. In the algorithm there is a fluid volume V^n calculated from the fracture width

$$V^n = \int_{S^+} W^n dS. \quad (77)$$

The hydrodynamics-elasticity problem in the algorithm in Fig. 45 provides the relation between the fracture width W^{n+1} and the pressure p^{n+1} which is produced by the fluid flow in the fracture in the crack front position $\mathbf{x}_{r_i}^{n+1}$ and the fluid front \mathbf{x}_f^n . The scheme of the solution algorithm for the hydrodynamics-elasticity problem is shown in Fig. 46. The iterative process $\Delta t^{k+1} = \mathbb{T}(\Delta t^k)$ is implemented to fulfill the condition

$$\max_i \left| \mathbf{v}_i^{n+1} \right| = v_f, \quad (78)$$

which provides the equivalence of the fluid velocity and the fracture front velocity $v_f = L_f^0 / \Delta t$, where Δt is calculated using the fracture volume dynamics.

References

- Abe H, Mura T, Keer LM (1976) Growth rate of a penny-shaped crack in hydraulic fracturing of rocks. *J Geophys Res* 81(29):5335–5340
- Aidagulov G, Alekseenko O, Chang F, Bartko K, Cherny S, Esipov D, Kuranakov D, Lapin V (2015) Model of hydraulic fracture initiation from the notched open hole. In: Proceedings 2015 annual technical symposium & exhibition, Al Khobar, Saudi Arabia, April 21–23, SPE-178027-MS, pp 1–12
- Alekseenko OP, Esipov DV, Kuranakov DS, Lapin VN, Cherny SG (2011) 2D step-by-step model of hydrofracturing Vestnik. *Quart J Novosib State Univ Ser: Math Mech Inf* 11(3):36–60 (in Russian)
- Alekseenko OP, Potapenko DI, Cherny SG, Esipov DV, Kuranakov DS, Lapin VN (2013) 3D Modeling of fracture initiation from perforated non-cemented wellbore. *SPE J* 18(3):589–600
- Aliabadi MH (2002) *The boundary element method: vol 2 (applications in solids and structures)*. Wiley, New York
- Barr DT (1991) *Leading-edge analysis for correct simulation of interface separation and hydraulic fracturing*. Massachusetts Institute of Technology, Department of Mechanical Engineering
- Blandford GE, Ingraffea AR, Liggett JA (1981) Two-dimensional stress intensity factor computations using the boundary element method. *Int J Numer Meth Eng* 17(3):387–404
- Briner A, Chavez JC, Nadezhdin S, Alekseenko O, Gurmen N, Cherny S, Kuranakov D, Lapin V (March 2015) Impact of perforation tunnel orientation and length in horizontal wellbores on fracture initiation pressure in maximum tensile stress criterion model for tight gas fields in the Sultanate of Oman SPE Middle East Oil & Gas Show and Conference, Manama, Bahrain, 8–11, pp 1–12, SPE 172663
- Briner A, Florez JC, Nadezhdin S, Gurmen N, Cherny S, Kuranakov D, Lapin V (September 2015) Impact of wellbore orientation on fracture initiation pressure in maximum tensile stress criterion model for unconventional gas field in the Sultanate of Oman. In: Proceedings of North Africa technical conference and exhibition, Cairo, Egypt, 14–16, pp 1–13, SPE-175725-MS
- Bueckner HF (1973) Field singularities and related integral representations. In: Sih GC (ed) *Mechanics of fracture, vol 1: methods of analysis and solutions of crack problems*. Nordhoff, Leyden, pp 239–314
- Carbonell R, Desroches J, Detournay E (1999) A comparison between a semi-analytical and a numerical solution of a twodimensional hydraulic fracture. *Int J Solids Struct* 36(31–32):4869–4888
- Carter BJ, Desroches J, Ingraffea AR, Wawrzynek PA (2000) Simulating fully 3D hydraulic fracturing. In: Zaman M, Booker J, Gioda G (eds) *Modeling in Geomechanics*. Wiley Publishers, New York, pp 525–557
- Carter BJ (1992) Size and stress gradient effects on fracture around cavities. *Rock Mech Rock Eng* 25(3):167–186
- Chang F, Bartko K, Dyer S, Aidagulov G, Suarez-Rivera R, Lung J (2014) Multiple fracture initiation in openhole without mechanical isolation: first step to fulfill an ambition. SPE-168638-MS, pp 1–18
- Chen JT, Hong H-K (1999) Review of dual boundary element methods with emphasis on hypersingular integrals and divergent series. *Appl Mech Rev* 52(1):17–33
- Cherepanov GP (1979) *Mechanics of brittle fracture (translated from the Russian by A. L. Peabody; ed. R. de Wit and W.C. Cooley)*. McGraw-Hill, London
- Cherny S, Chirkov D, Lapin V, Muranov A, Bannikov D, Miller M, Willberg D (2009) Two-dimensional modeling of the near-wellbore fracture tortuosity effect. *Int J Rock Mech Min Sci* 36(6):992–1000
- Cherny S, Esipov D, Kuranakov D, Lapin V, Chirkov D, Astrakova A (2015) Numerical method for solving a 3D problem of fracture initiation from a cavity in an elastic media presented in the international journal of fracture in 2015
- Cooke ML, Pollard DD (1996) Fracture propagation paths under mixed mode loading within rectangular blocks of polymethyl methacrylate. *J Geophys Res* 101(B2):3387–3400
- Crouch SL (1976) Solution of plane elasticity problems by the displacement discontinuity method. *Int J Numer Methods Eng* 10:301–343
- Cruse TA (1972) Numerical evaluation of elastic stress intensity factors by the boundary-integral equation method. *Surfasc cracks: physical problems and computational solutions*, pp 153–170
- Cruse TA (1973) Application of the boundary-integral equation method to three dimensional stress analysis. *Comput Struct* 3:509–527
- Desroches J, Thiercelin M (1993) Modeling propagation and closure of micro-hydraulic fractures. *Int J Rock Mech Min Sci* 30:1231–1234
- Dobroskok A, Ghassemi A, Linkov A (2005) Extended structural criterion for numerical simulation of crack propagation and coalescence under compressive loads. *Int J Fract* 133:223–246

- Erdogan F, Sih GC (1963) On the crack extension in plates under plane loading and transverse shear. *J Basic Eng* 85:519–525
- Esipov DV, Cherny SG, Kuranakov DS, Lapin VN (2011) Multiple-zone boundary element method modeling of hydraulic fracture initiation from perforated cased wellbore. In: Proceedings of international conference “Modern Problems of Applied Mathematics and Mechanics: Theory, Experiment and Applications”, devoted to the 90th anniversary of professor N. N. Yanenko (Novosibirsk, Russia, 30 May–4 June 2011). “Informregistr”. - Novosibirsk. - <http://conf.nsc.ru/files/conferences/niknik-90/fulltext/40532/47467/EsipovDV>
- Esipov DV, Kuranakov DS, Lapin VN, Cherny SG (2011) Multiple-zone boundary element method and its application to the problem of hydraulic fracture initiation from cased perforated wellbore. *Comp Technol* 16(6):13–26 (in Russian)
- Esipov DV, Kuranakov DS, Lapin VN, Cherny SG (2014) Mathematical models of hydraulic fracturing. *Comp Technol* 19(2):33–61 (in Russian)
- Germanovich LN, Cherepanov GP (1995) On some general properties of strength criteria. *Int J Fract* 71:37–56
- Goldstein RV, Salganik RL (1974) Brittle fracture of solids with arbitrary cracks. *Int J Fract* 10:507–523
- Gupta P, Duarte CAM (2014) Simulation of non-planar three dimensional hydraulic fracture propagation. *Int J Numer Anal Methods Geomech* 38(13):1397–1430
- Hong H-K, Chen JT (1988) Derivation of integral equations in elasticity. *J Eng Mech* 114(6):1028–1044
- Leblond J-B, Frelat J (2000) Crack kinking from an initially closed crack. *Int J Solids Struct* 37:1595–1614
- Leblond J-B, Frelat J (2001) Crack kinking from an interface crack with initial contact between the crack lips. *Eur J Mech A: Solids* 20:937–951
- Leblond JB, Frelat J (2004) Crack king from an initially closed, ordinary or interface crack, in the presence of friction. *Eng Fract Mech* 71:289–307
- Liu YJ, Li YX (2014) Revisit of the equivalence of the displacement discontinuity method and boundary element method for solving crack problems. *Eng Anal Bound Elem* 47:64–67
- Mi Y, Aliabadi MH (1992) Dual boundary element method for three-dimensional fracture mechanics analysis. *Eng Anal* 10(2):161–171
- Mi Y, Aliabadi MH (1994) Three-dimensional crack growth simulation using BEM. *Comput Struct* 52(5):871–878
- Murakami Y (Editor-in-Chief) *Stress intensity factors handbook*. Pergamon Press, Oxford (1987)
- Napier JAL, Detournay E (2013) Propagation of non-planar pressurized cracks from a borehole. In: Proceedings of the 5th international conference on structural engineering, mechanics and computation, SEMC 2013, pp 597–602
- Neuber HK (1937) Verlag Julius Springer, Berlin
- Novozhilov VV (1969) On a necessary and sufficient criterion for brittle strength. *J Appl Math Mech* 33(2):201–210
- Nuismer RJ (1975) An energy release rate criterion for mixed mode fracture. *Int J Fract* 11:245–250
- Paris A, Erdogan F (1963) A critical analysis of crack propagation law. *J Basic Eng* 85:528–534
- Pereira JPA (2010) Generalized finite element methods for three-dimensional crack growth simulations. PhD Dissertation in Civil Engineering, University of Illinois
- Portela A, Aliabadi MH, Rooke DP (1991) The dual boundary element method: efficient implementation for cracked problems. *Int J Numer Methods Eng* 32:445–470
- Richard HA, Fulland M, Sander M (2005) Theoretical crack path prediction. *Fatigue Fract Eng Mater Struct* 28:3–12
- Rizzo FJ (1967) An integral equation approach to boundary value problems of classical elastostatics. *Quart J Appl Math* 25:83–95
- Rungamornrat J (2004) A computational procedure for analysis of fractures in three dimensional anisotropic media. Ph.D. Dissertation, Department of Aerospace Engineering and Engineering Mechanics, The University of Texas at Austin
- Rungamornrat J, Wheeler MF, Mear ME (2005) A numerical technique for simulating nonplanar evolution of hydraulic fractures. Paper SPE 96968:1–9
- Savitski AA, Detournay E (2002) Propagation of a fluid-driven pennyshaped fracture in an impermeable rock: asymptotic solutions. *Int J Solids Struct* 39(26):6311–6337
- Schollmann M, Richard HA, Kullmer G, Fulland M (2002) A new criterion for the prediction of crack development in multiaxially loaded structures. *Int J Fract* 117:129–141
- Sedov LI (1997) *Mechanics of continuous media*. World Scientific, Singapore
- Sneddon IN, Elliott HA (1946) The opening of a griffith crack under internal pressure. *Quart Appl Math* 4:262
- Snyder MD, Cruse TA (1975) Boundary-integral equation analysis of cracked anisotropic plates. *Int J Fract* 11(2):315–328
- Sousa JL, Carter BJ, Ingraffea AR (1993) Numerical methods of 3D hydraulic fracture using Newtonian and power-law fluids. *Int J Rock Mech Mining Sci Geomech Abst* 30(7):1265–1271
- Tada H, Paris P, Irwin G (2000) *The stress analysis of cracks handbook*, 3rd edn. ASME Press, New York
- Vandamme L, Curran JH (1989) A three-dimensional hydraulic fracturing simulator. *Int J Numer Methods Eng* 28:909–927
- Watson JO (1982) Hermitian cubic boundary elements for plane problems of fracture mechanics. *Res Mechanica* 4:23–42
- Watson JO (1986) Hermitian cubic and singular elements for plane strain. In: Banerjee PK, Watson JO (eds) *Developments in boundary element methods - 4*, Chapter 1. Elsevier Applied Science Publishers, London, pp 1–28
- Weber W, Kuhn G (2008) An optimized predictor–corrector scheme for fast 3d crack growth simulations. *Eng Fract Mech* 75:452–460. doi:10.1016/j.engfracmech.2007.01.005 International Conference of Crack Paths